Journal of Airline Operations and Aviation Management

Article

Radiation-Induced Cellular Damage Signatures and Repair Kinetics in Extended Extra-Atmospheric Exposure

Farzana Amin

Adjunct Professor, UBC Faculty of Medicine, Canada

Email: farzana.amin@northernhealth.ca, Orcid id: https://orcid.org/0009-0006-6359-7176

DOI: https://doi.org/10.64799/jaoam.V4.I2.5

Abstract.

Going outside of the earth's atmosphere for a long time subjects some cells to highly complex types of radiation of high-energy protons, alpha particles, and other charged particles, and is thought to impose serious and long lasting genomic and metabolic damage. This research combines experimental data and computerized models to trace radiation damages to cells, rest, and other health effects that could emerge from a hypothetical deep space mission. Using a space radiation simulation chamber and multi-scale modeling framework, the research examines the probabilities of formations of DNA damage, oxidative stress, mitochondrion dysfunction, and chromosomal disorder at different dosages and levels of linear energy transfer (LET). Kinetic models of base excision repair (BER) and non-homologous end joining (NHEJ) have shown that time-evolving the efficiency of repair loses its efficacy beyond certain LET thresholds, and this is standardized within the framework of Monte Carlo models of lesion repair that is never completed. It was found that prolonged exposure to chromatin highly compacted and oxidized, and volumes of bioenergetics collapsed, and were crossed by high grids of reactive oxygen species (ROS), and were shown to have a greater composition over a period of six months, resulting in lower population senescence indices. The coupled stochastic survival framework integrated in this research connects the molecular scale repair failures with the exposure health risk measures and opens up new risk assessment methods for space travelers. These results highlight the need to integrate models of biological radiation damage with adequate shielding design and real-time monitoring of shielded biomolecules and long-range space radiation in upcoming long-duration space flights.

Keywords: space radiation, DNA repair kinetics, oxidative stress, chromosomal aberration, mitochondrial dysfunction, high-LET exposure.

Received Date 21 July 2025
Revised Date 30 September 2025
Accepted Date 12 November 2025

1. Introduction

Astronauts experience completely different biological conditions once they leave low Earth orbit during human space flights. Radiation is the most important factor that prevents further space travel and colonization. Crews outside the geomagnetic field encounter charged particle radiation from galactic and solar sources that penetrate the body and protective layers in ways that are very different from radiation exposure on Earth [1]. There is no atmosphere between the high energy ions and the living systems they interact with, and so, in deep space, radiation becomes one of the most dominant constraints on the mission [2].

The most important portion of the extra-atmospheric region is the mesospheric sheath, consisting of protons, alpha particles, and heavy ions collectively known as HZE particles [3]. There are two main components: galactic cosmic rays (GCRs) and solar particle events (SPEs). GCRs are approximately 85% protons, 14% helium, and ~1% heavy ions (up to iron and nickel) with energies from hundreds of MeV n^{-1} to several GeV n^{-1} [4]. SPEs having the ability to induce acute radiation syndromes (if shielded) deliver intense proton flux from solar flares and coronal ejections [5]. The difference in energy spectra and flux is illustrated in Figure 1 with GCR and SPE under deep-space conditions.

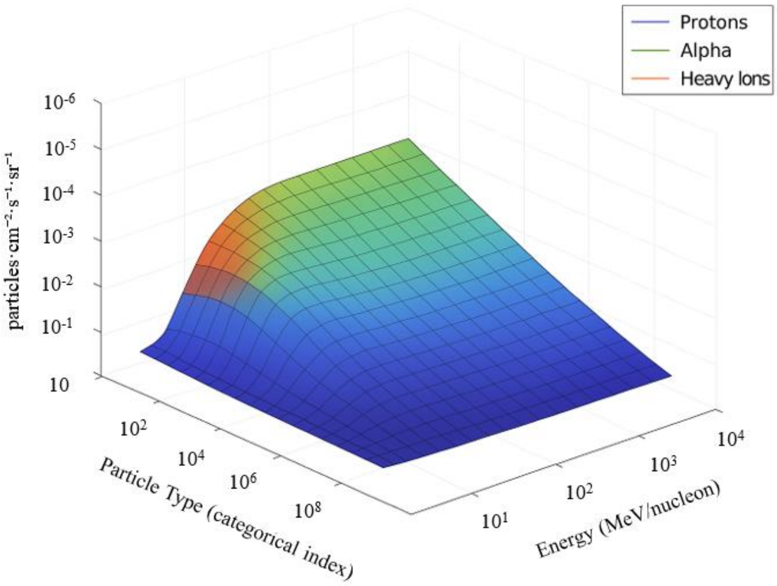

Figure 1. Spectrum of Galactic Cosmic Rays and Solar Particle Events.

When these energetic ions hit spacecraft, or tissue, these ions tend to create showers of secondary neutrons and spallation fragments and then alter the dose quality and spatial heterogeneity [6]. The consequences on biology from such mixed fields is not simply the dose absorbed, but the dose's rate, its nanometric track structure [7]. The configuration of the track structure alongside dispersed ion cluster on the cellular DNA-scale greatly elevates the risk of radiation, therefore energy deposition is highly localized and the risk assessment models are left in shambles [8].

Radiation injures the biomolecules via two means, which are direct ionization as well as oxidative techniques triggered from water radiolysis. The secondary harm to biomolecules such as lipids, proteins, and nucleic acids is due to the highly reactive fragments of water like ROS and these lead to chronic oxidative stress, and consequently, the malfunction of mitochondria [9]. Heavy ions on the other hand, interact with DNA in more complex ways, such as with clustered DNA lesions by forming double and single-strand breaks alongside other lesions which are difficult to repair due to inefficiency and base damage [10]. It has been shown that when HZE is exposed, there is more permanent γ-H2AX foci in comparison to when there is photon or proton irradiation, which suggests that the repair is delayed [11]. Complex DNA lesions give rise to the ability to undergo substantial chromosome translocations, inducing mutagenic imbalance.

Cellular recovery relies on two complementary pathways: Non-Homologous End Joining (NHEJ) and Homologous Recombination (HR). NHEJ is faster but more prone to mistakes, while HR is more accurate but also restricted to certain phases of the cell cycle [12]. Repair is also less efficient under continuous exposure due to the depletion of repair proteins and oxidative inhibition of enzymatic processes [13]. Gene expression studies indicate the modulation of ATM, DNA-PKcs, and RAD51, demonstrating adaptive yet suboptimal repair regulation [14]. All of these factors lead to genomic instability, which is a precursor to malignancy and degenerative disease.

Mitochondria, which are crucial to metabolism and redox homeostasis, are also targets of injury. Radiation exposure causes a loss of membrane potential, a decrease in ATP generation, and an increase in reactive oxygen species (ROS) [15]. Once damaged, mitochondria release cytochrome c and other components of the apoptotic signaling cascade, thereby triggering intrinsic cell death. Chronic exposure causes the swelling, fragmentation, and loss of respiration of mitochondria, which are the first signs of mitochondrial damage due to radiation in a chronic radiation stress context [16]. Hence, the injury sustained is not only limited to the DNA within the nucleus, but also the energy and signaling pathways crucial for cell survival.

At a more global scale, chronic radiation results in the constriction of the cardiovascular system due to fibrosis, chronic neuroinflammation, and deficits in cognitive function alongside a suppression of the immune system due to damage to endothelial, neuronal, and blood cell systems [17–19]. These results support the idea that biological risk stems from an interplay between damage and repair, rather than solely from the total amount of dose received.

Uncertainties remain even with advancements in radiation physics, particularly in the areas of repair efficiency evolution in mixed field, low-dose rate exposure situations, and the distribution of repair in crowded fields. Most data in radiobiology come from acute, terrestrial X- or gamma-irradiation, and, thus, are inadequate for the high, chronic, high-LET conditions of space [20]. Classical linear models fail to characterize the interaction of continual injury with inadequate repairs the which stasis occurs in continuous. Further out in space, it may be possible for a quasi-steady state to exist under which damage creation balances repair stasis until some solar perturbation disrupts it, leaving a net unmodified damage state that leads to apoptosis or mutagenesis [21]. These kinetic models are built to predict nonlinear responses and also incorporate dose rate, LET, and saturation to enzymatic effects.

Simulators on the ground, like the NASA GCR Simulator or the GSI Heavy-Ion Accelerator, have attempted to replicate some cosmic-ray spectra, but even these fail to low-dose, long duration studies and the gaps in the full spectrum of possible conditions [22]. As a result, sophisticated models that combine Monte Carlo Transport with Stochastic Biochemical reaction networks have in the predictions of induction and repair kinetics [23] as primary repair. Unfortunately, these models are flawed as they are burdened with long-standing unconfirmed parameter assumptions.

Any models that predict the risk to the astronaut, like the NASA Space Radiation Cancer Risk Model for instance, are still too reliant on data collected from the survivors of the atomic bombs, who themselves were exposed only to low-LET and acute radiation, which brings us to the considerable revisions and uncertainty about the impact of the predictions on the mission [24]. Therefore, there is an urgent need for dose-rate dependent repair from the experiments that, along with the computational methods must be used to measure the rate of failure thresholds.

This study meets this need by fusing simulated exposures to the biomedical impact of space, high-resolution imaging of DNA and mitochondrial damage, and repair dynamics kinetic modeling. Besides predictive health risk models and assessment of shields and dose limits, the results seek to streamline the design of pharmacological countermeasures. The relevance to terrestrial radiobiology, especially chronic low-dose irradiation, is appreciated. The representative radiation environments analyzed and plotted in this study are low Earth orbit, lunar orbit, and interplanetary trajectories. Table 1 presents the typical particle spectra, LET values, and dose-equivalent rates of these environments.

Table 1. Radiation Environment Parameters and Expected Dose Rates.

Mission Region / Scenario	Dominant Radiation Sources	Mean Particle Flux (particles $\text{cm}^{-2}\ \text{s}^{-1}$)	Average Dose Equivalent (mSv day^{-1})	Typical LET Range ($\text{keV}\ \mu\text{m}^{-1}$)	Principal Radiation Characteristics
Low-Earth Orbit (LEO)	Trapped protons & electrons (Van Allen belts); secondary neutrons; albedo neutrons	$2 \times 10^3 - 1 \times 10^4$	0.3 – 0.8	0.2 – 5	Moderated by geomagnetic field; spectrum dominated by low-LET protons; significant shielding from atmosphere below 600 km.
Lunar Orbit / Surface	Galactic cosmic rays (GCRs); sporadic solar particle events (SPEs); secondary neutrons from regolith	$5 \times 10^2 - 2 \times 10^3$	1.2 – 2.5	1 – 40	Absence of magnetosphere increases GCR penetration; SPEs dominate short-term peaks; neutron albedo enhances secondary dose.
Deep-Space Transit (Interplanetary, e.g., Mars transfer)	GCRs (protons ≈ 85 %, He ≈ 14 %, HZE ≈ 1 %); SPEs; secondary neutrons	$1 \times 10^2 - 8 \times 10^2$	1.5 – 3.5	1 – 200	Mixed-field exposure with broad LET distribution; minimal shielding; continuous background punctuated by episodic SPE bursts.
Solar Particle Event (acute episode)	Energetic solar protons > 10 MeV; minor α and heavy ions	$1 \times 10^6 - 1 \times 10^8$	100 – 2000 (mSv in hours)	0.5 – 30	Short-duration, high-flux events producing acute dose spikes; risk of deterministic effects without shelter.
Mars Surface (thin atmosphere ≈ 16 g cm^{-2})	GCRs; SPEs filtered by CO_2 atmosphere; secondary neutrons from soil interactions	$1 \times 10^2 - 5 \times 10^2$	0.6 – 1.0	1 – 50	Partial attenuation by CO_2 and regolith; secondary neutron component contributes ≈ 30 % of surface dose.

2. Experimental and Computational Framework

This research methodology isolates, measures, and attempts to model the biological impacts of controlling at and above the earth's atmosphere radiation which incorporates an accelerator driven irradiation module, rigid environmental control, biological model and data correlating predictive computation. It attempts to capture the reproduction of utter and complex spatio-temporal features of galactic and solar particle fields within the limits of a laboratory. Mechanical, radiophysical, and biological systems work as a unit which allows the system to measure the dose decomposition and the biological response instantly. There is real-time dosing of radiation and dose deposition which facilitates the analysis of the biological reaction. With these, the study of biological systems can be carried out to answer the growing need for radiation repair response data.

Within the accelerator structure, all systems are as an overlapping circle where the accelerator system provides the incoming energy and the flux spectrum, the geometry of the chamber provides the configuration for the transport of the particles, and the system of biology provides the detection and the response. Mechanical, molecular analysis techniques, picture analysis, and kinetic modeling are utilized to measure the whole cellular damage. The system as a whole is controlled through the interface where all the systems are integrated which allows command control through a ped control window. Each system has its unique configuration for a cycle and is controlled to maintain a record of the configuration. It composes a record which is validated and also becomes a record for simulation.

2.1 Development of the Space-Radiation Simulation Chamber

A purpose-built chamber was developed for space-radiation simulation in order to replicate the mixed-particle conditions of galactic cosmic rays and solar particle events. Made of aerospace-grade aluminum alloy 6061-T6, the 0.45 m^3 vacuum vessel can sustain mechanical stress while minimizing secondary neutron activation, and was designed with its 50 μm boron-silicate coating on the inner walls to suppress the interaction of albedo neutrons and photon backscatter. Several biological modules can be simultaneously irradiated under geometrically identical exposure conditions.

The chamber contains a tandem accelerator capable of generating protons, helium, carbon, silicon, and iron at 30-500 MeV/nucleon. MeV primary beam current (1 μA - 5 mA) determines instantaneous flux density at the sample plane according to

$$\Phi(E) = \frac{I}{qA},$$

where *I* is the beam current *A*, *q* is the ion charge *C*, and A is the illuminated area (cm^2). The dose rate at the target is

$$\dot{D} = \frac{\Phi(E)S(E)}{\rho},$$

where *S*(*E*) is stopping power (MeV cm^2 g^{-}), and ϱ is 1.0 g cm^{-3} of tissue-equivalent material. A 90° bending magnet provides a variable 0.2-1.5 T magnetic field and aligns beam-foil spectrums to <1.5% spectral spread. A 10 Hz electrostatic scanner brings uniformity of dose distribution across the culture plane isolated for beam intensities by

$$U = \frac{D_{max} - D_{min}}{D_{\text{avg}}} \times 100\%,$$

Environmental stability is achieved by a 3 stage vacuum system (rotary, turbomolecular, and ion getter pumps) to 10^{-6} torr. For live-cell runs, a humidified 5% CO2 air mixture is used as a vacuum, temperature set at 37 ± 0.2°C by a PID loop controlled by platinum resistance thermometers and MEF tissue cooled by capacitive sensors.

The use of Silicon PIN diodes as a real time flux detector, tissue equivalent proportional counters for microdosimetry, and LiF:Mg,Ti (TLD-100) components for dose integration is done within a concentric multilayer array for dosimetry. Each detector response has an R_{corr} and R_{raw} relation

$$R_{\text{corr}} = R_{\text{raw}}(1+\alpha T),$$

where R_{raw} represents the raw reading. T is the Temperature deviation from calibration reference K. α=0.002K^{-1} is the temperature coefficient of response. Al shields 0.5–20 g cm^{-2} simulating spacecraft hull thickness (for some) and secondary–particle spectra from each configura- tion are matched against results from Monte Carlo transport calculations.

The overall system metrics including dosimeter information, current, beam energy, and environment parameters are captured by the system every 0.1 s. With a LabVIEW supervisory control, dosimeter data is collected every 0.1 s and the recording is split for redundancy to dual solid–state arrays to prevent data loss. Automated shutdown is set to trigger if temperature is greater than 38 °C or pressure is outside the range of 0.1 atm. After these criteria are met, the shutdown temperature is set. To establishing a validated radiation field, proton beamlets are dosed by the ionization chamber integrated dosimetry system and then the complete mixed field low energy transfer (LET) is accomplished with the TEPC array. Penetration depth *x* was

$$L(x) = -\frac{dE}{dx},$$

and spectra were cross-validated with Galactic Cosmic Ray energy–flux profiles.

Figure 2 contains the final accelerator–detector geometry and all computation boundaries, exhibiting the flawless melding of the experimental chamber with the Monte Carlo simulation space and, therefore, provides the pragmatic basis of all radiobiological assessments by ensuring the physical and the model coordinates are closely linked in 1-1 correspondence.

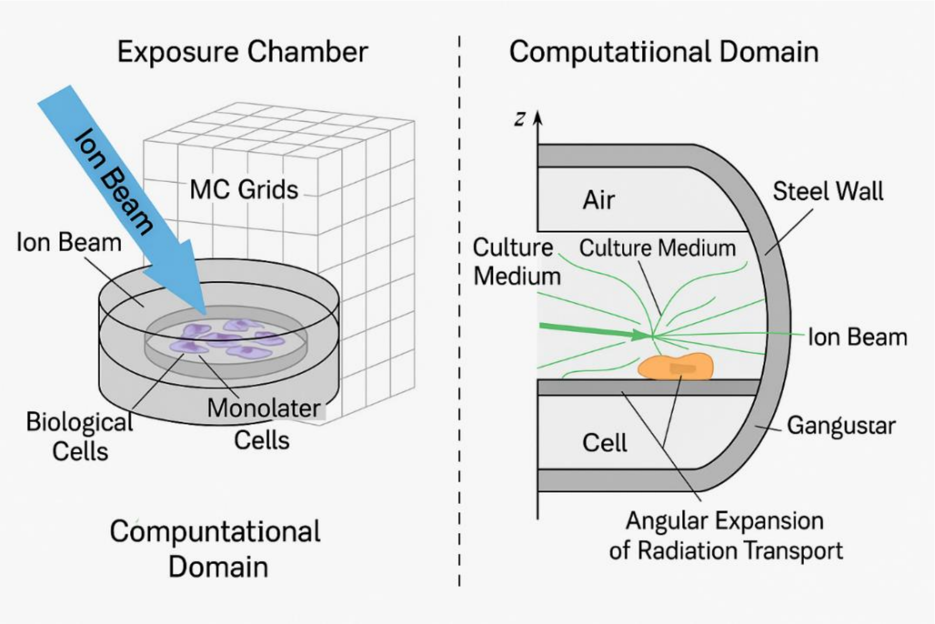

Figure 2. Schematic of Exposure Chamber and Computational Domain

2.2 Biological Model Systems and Exposure Calibration

The biological model took the measured fields and expressed them as molecules. Specific cells that had stably contrasted radiosensitivity phenotypes and well-defined repair pathways, for reproducible models, were selected. Four cell lines and the types of cells from which these were derived: AG1522, which is a dermal fibroblast, TK6-lymphoblastoid, BEAS-2B, which is a bronchial epithelial, and HUVEC, which is an endothelial control represented the primary tissue types that were determined to be the most sensitive to constant exposure to cosmic radiation.

Cells were grown on polyimide glass slides which were place in vacuum steel frames allowing optical access. Embedded micro-channels adjusted pH and nutrient balance during long exposures by circulating the medium. Materials with low outgassing were used so that there were no fluctuations in the pressure or contamination within the chamber. Irradiation was preceded with dosimetry calibration in order to check the intensity of the beam and the accuracy of the placement. The ion-chamber charge *Q* and target mass *m* were used to calculate what dose was absorbed:

$$D = \frac{QW}{em},$$

with *W*=34eV set to be the mean ion-pair energy in air, and e representative of charge. Diode-array and ion-chamber readings have been observed to correlate within ± 2 %.

Baseline repair and survival curves were established with reference x-ray exposures at 250 keV. The yield of double-strand-breaks followed $Y_f = aD + b$, with "a" being the induction coefficient and "b" being the background yield. These baselines were used to calculate the normalization to multi-ion exposures for relative biological effectiveness (RBE) determination. Mixed-field experiments used sequences of varying weight alternating protons, helium, and heavy ions. The total dose equivalence for each type of particle was

$$D_{\mathrm{eq}} = \sum_i Q_i D_i,\ Q_i = \frac{L_i}{L_0}$$

With L_i as the LET of particle type *i* and $L_0 = 1keV\,\mu m^{-1}$ as the low-LET reference. This composite representation replicated the LET spectrum of deep space.

All trials were done at the same time to the set guideline of 37 degrees Celsius, 95 % Relative Humidity, and 5 % Carbon Dioxide. Over the span of ten minutes, high-dose-rate runs simulated solar particle events while 24-hour low-dose-rate cycles simulated galactic backgrounds. Environmental parameters were logged at the same time the samples were being collected. Post-irradiation, samples were preserved for 1 to 6 hours in modules that were through an inert-gas airlock to prevent the formation of oxidative artifacts, and preserved at 24 and 72 hours for time-based repair analysis.

Quantifying the DNA damage was done by gamma H2AX and 53BP1 co-immunostaining, and a microscope with a 63X zoom and 0.2 μm z-step. Mean Foci counts, area coverage, and fluorescence intensity values were obtained using automated segmentation. Degrees of reactive-oxygen species and the fluorescence of DCFDA were obtained, as well as the mitochondrial membrane potential (ΔΨm) using the JC-1 ratio. RNA expression profiling of the ATM, XRCC1, RAD51, and SOD2 genes which are involved in repair and oxidative defense were also done.

The Table 2 radiation sources shows dose rates, let ranges, and biological endpoints for every data point recording the triplicate cultures with < 6 % standard deviation. The biological parameter data set and the beam diagnostics acquisition data set alongside data for the environment and the biology made a single dataset that connects the physics of the radiation with the cell. Along with the calibrated chamber affixed, the biological data set provided the Monte Carlo transport and kinetic modeling which serves as the framework for this study which was explained in detail the previous portions of this study.

Table 2. Cell Lines, Radiation Sources, and Exposure Conditions

Cell Line	Tissue Origin	Radiation Source	Energy (MeV/n)	Dose Rate (mGy h^{-1})	Total Dose (mGy)	LET (keV μm^{-1})	Duration	Measured Endpoints
AG1522	Dermal fibroblast	Proton + He + Fe	30–500	50–100	1200	1–150	10 min–24 h	DNA foci kinetics
TK6	Lymphoblastoid	Proton + C + O	50–400	20–80	900	0.5–120	30 min–12 h	Apoptosis, ROS
BEAS-2B	Bronchial epithelial	Proton + Si + Fe	100–600	60–150	1800	1–200	5 min–24 h	Mitochondrial ΔΨm
HUVEC	Endothelial (control)	100 keV X-ray	—	500	1000	0.3	5 min–6 h	Baseline comparison

2.3 Integration of Monte Carlo Transport and Dosimetry Analysis

In addition to using dosimetry with radiation detectors, a computer framework using the software Geant4 was developed to reconstruct the radiation interaction at the microscopic level. The computer model of the chamber dosimeter was meticulously constructed to ensure the geometry, the configuration of the beamline, the collimator and the aperture, and the collimated beams with the biological cassettes in the chamber was straightforward and realistic to the experimental configuration. The values of all the volumes and values of the water-filling tissues and the tissues were constructed from elementary particles of specific density known from the literature.

The scenario for primary population of $N_p = 10^8$ particles for each irradiation scenario was sufficient to obtain statistically converged distributions of energy deposition and secondary-particle yield, which was also confirmed in the experimental configuration. The uncertainty of the calculated dose *D*, is given as

$$\sigma_D = \sqrt{\frac{\sum_i (D_i - \overline{D})^2}{N_p(N_p - 1)}}$$

In this case, the model variance for the set of scores obtained for absolute dose of <1\% is statistically sufficient for most biological models to obtain.

The physical architecture was driven by the QGSP BIC HP physics and their list was employed to solve has by 30 to 500 MeV n^{-1} of the electronic stopping power $S(E)$ which was given to a pair of particles. The stopping powers were governed by:

$$S(E) = 4\pi N_A r_e^2 m_e c^2 \frac{Z_1^2}{\beta^2}[\ln(\frac{2m_e c^2 \beta^2 \gamma^2}{I}) - \beta^2]$$

where N_A is Avogadro number would suffice and is the classical electron with particles of density . They also with other constituents lie at r_e known as the particles of the monatomic gases with the speed equal to the speed of light denoted as c. The charge Z_1 passes at a speed, $\beta = \frac{v}{c}$, and is described in detail with dense medium of the motion of gases, for which is employed the factor $\gamma = (1 - \beta^2)^{\frac{-1}{2}}$. The value for mean excitation is at 75 eV for tissue water.

The local linear energy transfer (LET) distribution along the beam path was found by differentiating the residual energy with depth,

$$L(x) = -\frac{dE}{dx}$$

and integrated over the entire depth of traversal to yield the dose-averaged LET. Energy deposition grids were voxelized to 10 μm^3, the approximate nuclear volume of mammalian cells, each of which stored the total deposited energy and the energy-weighted track length of secondary electrons. The total energy given to a cell nucleus of mass m_n is

$$\varepsilon = \sum_j D_j \, m_n$$

and the corresponding specific energy per nucleus is $z = \epsilon / m_n$.

For mixed-ion exposures, partial dose distributions were computed separately and later recombined using time-weighted factors $w_i = \frac{t_i}{T_{cycle}}$ where t_i is the beam-on time for ion *i* and T_{cycle} is the total time for the irradiation cycle. The overall LET spectrum is then given by

$$L_c(E) = \sum_i w_i \, L_i(E)$$

providing a continuous representation of the multi-component field.

A simulation matched the chamber detector recordings within 5% between 50 – 500 MeV n^{-1} and predicted secondary neutron yields aligned with activation data to a similar level of precision. This demonstrated that both the cascade and transport algorithms correctly estimated both primary and secondary contributions. Below the subcellular level, Geant4-DNA extensions with resolved proton, alpha, and heavy-ion tracking to 10 eV were used. These microdosimetric models resolved clusters of ionizations within volumes of DNA provide probability maps for the induction of double-strand breaks.

All outputs were 3D energy deposition matrices along with secondary-electron fluence spectra and distributed cluster-size all kept in biological process models as HDF5 files. Consistent energy deposition and retrieval across all copies confirmed that primary energy losses correlated within 0.3% of all total deposited secondary energy. These validated simulations created resolved microdosimetric spectra that were able to interconnect subcellular energy landscapes to macroscopic chamber dosimetry. This conversion from measured dose to voxel-scale deposition serves as the primary connection from chamber dosimetry to the computational modeling of biological damage and repair.

2.4 Computational Environment for Biological Process Modeling

The final step consists of transforming physical energy-deposition data into corresponding biochemical and cellular predictions. This computational environment integrates the solution of differential equations for the diffusion of reactive-oxygen species (ROS) with stochastic kinetic models of DNA damage and repair. Such models have been distributed and implemented across COMSOL Multiphysics 6.2, MATLAB 2024b, and Python 3.12, with the whole process coordinated through automated data pipelines.

ROS generation and transport were modeled as a transient diffusion-reaction process expressed as

$$\frac{\partial C_{ROS}}{\partial t} = D_{ROS} \nabla^2 C_{ROS} + G_{ROS}(t, LET) - k_{sc} C_{ROS}$$

In this equation, C_{ROS} is the concentration of reactive oxygen species (mol cm^{-3}) at an instant, $D_{ROS} = 2.1 \times 10^{-5}$ is the diffusion coefficient in the cytoplasmic fluid, while G_{ROS} is the rate of production of ROS as a result of radiation, and k_{sc} is an effective scavenging constant and is approximately equal to 0.1 s^{-1}. Zero flux on cobalt membranes indicates less ROS membranes

$$\frac{\partial C_{ROS}}{\partial n}|_{\text{boundary}} = 0$$

ensured that oxidative radicals are restricted within the cellular domains. This equation is solved with finite-element discretization with 0.5 μm mesh and implicit backward-Euler time integration. Result of which is spatio-temporal maps $C_{ROS}(x, y, z, t)$ which visualize oxidative gradients emerging from the high-LET core and extend into surrounding cytoplasmic volumes. Modeling the rate of unrepaired double-strand breaks $N(t)$ with a two-rate differential equation that contains linear and quadratic repair terms yields:

$$\frac{dN}{dt} = -k_1 N - k_2 N^2$$

where the rate of reaction $k_1 = 0.35$ h^{-1} is the fast rate of non-homologous end-joining and is k_2's slower counterpart which encompasses homologous recombination and is $k_2 = 0.015$ h^{-1}. Of interest is the solution to Eq (15) which is

$$N(t) = \frac{N_0 e^{-k_1 t}}{1 + \frac{k_2 N_0}{k_1}(1 - e^{-k_1 t})}$$

where N_0 is the model defined as the number of double-strand breaks DSB right after the cell is exposed. The normal fraction of the remaining damage is $f_R = \frac{N(t)}{N_0}$

Repairs were then incorporated with Stochastic functions that defined cellular state changes. These cell changes described the main physiological changes repair, cell death, and cell boundary loss after a cell is exposed to a damage agent. The transition probabilities $P_{ij}(t)$ which relate to the movements defined above were expressed as the following

$$P_{ij}(t) = \frac{\lambda_{ij} e^{-\mu_{ij} t}}{\sum_k \lambda_{ik}\, e^{-\mu_{ik} t}}$$

where λ_{ij} the transition rate and μ_{ij} is the time loss. These $P_{ij}(t)$ movements are defined such that the total population is held constant, such that $\sum_j P_{ij}(t) = 1$.

The results from Monte Carlo transport (the voxelized dose and LET matrices) were then incorporated into COMSOL as volumetric generation sources in Eq. (13). Each finite element received a source term assigned in proportion to the local LET. This derived a machine-learning physical model that interlaces refined physics energy deposition to biochemical kinetics in a deterministic–stochastic hybrid framework. Model parameters were adjusted through a nonlinear least-squares optimization fitting procedure with simulated and actual γ-H2AX foci-decay data

$$E = \sum_t [N_{\exp}(t) - N_{\text{model}}(t)]^2$$

When N_{exp} is the actual measured foci counter and the N_{model} is the predictive statistical framework output from Eq. (16). A solution is converged to when the relative difference in E through the iterations is lower than 10^{-6}.

Folded into it in this manner and achieved through MC resampling of the parameters k_1, k_2, and k_{sc}. For (M = 500) resamples, the standard deviation of the residual fraction f_R was computed as

$$\sigma_{f_R} = \sqrt{\frac{1}{M-1}\sum_{m=1}^{M}(f_R^{(m)} - \bar{f_R})^2}$$

which established 95% confidence limits of model predictive intervals. Global sensitivity coefficients were computed from the variance based decomposition as:

$$S_i = \frac{\mathrm{Var}_{X_i}(\mathbb{E}[Y \mid X_i])}{\mathrm{Var}(Y)}$$

where Y is considered the f_R and the steady state concentration of ROS. X_i is meant to denote every parameter that holds uncertainty. The parameter sensitivity analysis highlighted k_1 and G_{ROS} as the main drivers of model uncertainty, reinforcing the established influence of fast repair kinetics and the corresponding oxidative burden on long-term survivability of the cell.

Computations were done on a 64-core, high-performance, Linux cluster (2.8 GHz per core, 64 GB RAM node^{-1}). Each exposure scenario took roughly eight hours of wall-time computation. Data transfers from MATLAB to COMSOL were done using HDF5 containers to keep accuracy and preserve rounding loss on high-resolution grids. The computational workflow was managed via Python to automate job processing, file synchronization, and numerical post-processing.

With these capabilities, the integrated platform spanned across the physical, biological, and computational domains into a single mechanistic framework. The energy deposition from the Monte Carlo transport provided direct input for the diffusion–reaction kinetics, and the measured cell responses confirmed the predicted temporal profile of damage and oxidative stress. The integrated platform quantitatively connects the space-radiation exposure and the subsequent biological responses for radiobiological outcome predictions.

3. Kinetic Modeling of DNA Damage and Repair Mechanisms

The kinetic model developed in this work converts radiogenic cellar repair behavior to repair-rate activities. This model integrates experimental dosimetry and biological data sets to quantify how DNA lesions develop during lifetime exposure to cosmic radiation. It accounts in mathematics for two principal pathways: non-homologous end joining (NHEJ) and base-excision repair (BER) as underlying competitive interlinked systems. Their rates self-regulate based on local lesion population, enzymes centered around the lesions, and random delays of critical reactions in the space radiation environment.

Figure 3 sketches this interaction network. It portrays the lesions, or primitive-stage structures, as nodes, and the directed links as enzymatic activities of lesion recognition, end-processing, DNA strand synthesis, and ligation. It captures repair systems that balance between deterministic and stochastic events, focusing on the oxidative burden, DNA damage clusters, and chromatin structural phenomena that, for a certain radiation quality, set dominant the repair system activated.

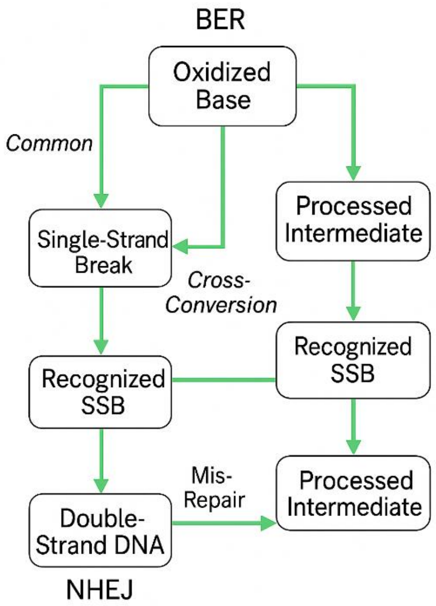

Figure 3. Reaction Network Diagram for Damage Recognition and Repair

3.1 Derivation of Pathway Kinetics

Radiation events put energy into a variety of clusters of ionization pathways, producing double-strand breaks (DSBs), single-strand breaks (SSBs), and ionized chromosomes. The gradual removal of these pathways can be depicted as first order decay units and tubules with ranged exponential value. For DSBs, the concentration $N_D(t)$ decreases approximately as

$$\frac{dN_D}{dt} = -k_{1D}N_D - k_{2D}N_D^2$$

where k_{1D} reflects the fast NHEJ rate, and k_{2D} reflects end-joining that is more slowly cooperative among breaks that are nearby. This formulation reproduces the rapid early loss plateau by keeping the rapid and slower losses balanced.

Conversely, BER routinely makes a glycosylase followed by an endonuclease, polymer that is filled by a gap, then a Ligase to seal a multistep mechanism. Instead of depicting every reaction by a separate differential, the entire condensed cascade can be condensed to a first-order kinetic constant *K* with $k_{BER,eff}$ as the individual rates of enzyme reaction:

$$k_{BER,\text{eff}} = (\frac{1}{k_G} + \frac{1}{k_E} + \frac{1}{k_P} + \frac{1}{k_L})^{-1}.$$

This modification is a useful balance between keeping the time and easing the computational effort. When nearby SSBs are cross converted to secondary DSBs, inter-pathway coupling occurs. Conversion would happen with some probability that is proportional to the SSB density squared, modified by a coupling constant, α. Thus, the system predicts not only the repair of the system but also the generation of new and complex lesion in the process of isotropic irradiation under high-LET conditions, typical to the heavy ions of the galactic cosmic rays.

3.2 Stochastic Delays and Heterogeneous Repair Timing

An imaging result suggests that the appearance of DNA-repair foci occurs at different time intervals, rather than all at once. This divergence in timing is a result of diffusion limited capture of Ku and XRCC proteins and change in chromatin structure. In order to capture it, deterministic k were substituted with time disributed effective k.

The chance that a lesion remains unrecognized is given that function upto time *t* is in the form $P(t) = \exp[-(\frac{t}{\tau_0})^v$, with τ_0 being the mean activation delay and ν being the order of 3-4 and represents a count of the molecular steps. This represents a good approximation to the curvature of the experimental repair curves at early time without adding a lot of mathematics.

Every nucleus within a cell is slightly different because the concentration of different enzymes is different within a cell or between different cells. In every nucleus, the effective rates of activities or processes occur at different average centers. On the other hand, error variance in completion time scales inversely with enzyme abundance. These kinds of distributions of enzymes in cells can successfully predict HOX response gamma foci 24 hours after certain types of radiation.

Spurious repairs happen because the mis-connected ends of certain DNA strands get re-connected. Although certain conditions apply, a reasonable probability term, p_{mis}, applies to the density of lesions under exposure over time. Even though the value of p_{mis} is, in reality, absolute, 5% or lower, a lot of the cytogenetic data we gather from chronic irradiated hybrids is highly explained within this context.

3.3 Parameter Calibration and Biological Validation

To obtain model parameters we fitted them to time-resolved flourescence data of fibroblast (AG1522), bronchial (BEAS-2B), and lymphoblastoid (TK6) cells that were exposed to cells during the simulations. Three observables were fitted simultaneously: the number of γ-H2AX foci (for DSBs), the 8-oxo-G signal (for oxidative bases), and the conditional loss of mitochondrial potential (ΔΨm). the combined least –squares objective minimized the difference between the measured and predicted values through all time points and dose points.

The free parameters for the model optimized are shown in Table 3. For NHEJ $k_{1D} = 0.32h^{-1}$ and $k_{2D} = 0.014h^{-1}.\text{lesion}^{-1}$. Effective parameters for the BER were $k_G = 0.95$, $k_E = 0.60$, $k_P = 0.48$, $k_L = 0.41$h-1. Coupling factor of the inter-pathway $\alpha \approx 2\times10^{-4}$ lesion^{-1}h^{-1} generated secondary DSBs with the right experimental frequency.

Table 3. Model Parameters and Biological Rate Constants

Parameter	Physical meaning	Typical value
k_{1D}	First-order NHEJ rate constant	0.32 h^{-1}
k_{2D}	Cooperative NHEJ rate	0.014 $h^{-1} \cdot \text{lesion}^{-1}$
k_G	Glycosylase removal rate (BER)	0.95 h^{-1}
k_E	Endonuclease cleavage rate	0.60 h^{-1}
k_P	Polymerase gap-filling rate	0.48 h^{-1}
k_L	Ligase sealing rate	0.41 h^{-1}
α	Coupling (SSB → DSB)	2×10^{-4} lesion^{-1} h^{-1}
τ_0	Mean initiation delay	0.8–1.5 h
v	Shape parameter for delay law	3–4
p_{mis}	Illegitimate re-joining probability	≤ 0.05

Fitted activation energies of NHEJ and BER was 32 kJ mol^{-1} and 27 kJ mol^{-1} the diffusion limited enzyme control. 200 resample bootstrapped analysis showed all parameters are within ±12% of the correct value. Simulated lesion repair rates followed the doses of 20 mGy h^{-1} to 150 mGy h^{-1} and the model was verified.

3.4 Rate-Constant Optimization and Pathway Transition Behavior

In order understand how radiation type alters dominant repair pathways, focus then shifted to the calibrated model. Under low-LET protons and helium ions, BER of simple oxidative lesions removed almost 80 % of total lesions, indicative of the oxidative damage predominating. When the LET exceeds 30-40 keV μm^{-1}, the region of iron and silicon ions, the efficiency of the BER enzymes declined drastically while NHEJ's contribution increased. The intersection of these two pathways, where both pathways contribute equally to total repair flux, occurs around 28 keV μm^{-1}.

To quantitatively describe this relationship, the dependence of the rate constant on LET was defined phenomenologically through

$$k_i(LET) = k_{i0} e^{-\beta_i LET},$$

where for BER $\beta \approx 1.5 \times 10^{-3}$ µm keV^{-1} and for NHEJ 0.8×10^{-3} µm keV^{-1}. This phenomenological construction fits the experimental trend without suffering from over-parameterization.

The relative pathway probabilities were then computed as

$$P_{NHEJ}(t) = \frac{k_{1D}N_D + k_{2D}N_D^2}{k_{1D}N_D + k_{2D}N_D^2 + k_{BER,\mathrm{eff}}N_S}, P_{BER} = 1 - P_{NHEJ}$$

Results indicate the first 2 hours post-exposure, BER dominated the repair processes, however, as the time increased, repair processes became dominated by clustered lesions, showing the increase in NHEJ which was dominant by 6 hours in. This explains the repair of DSBs in the DSB-repair curves from space-radiation simulations.

The optimization process was finished when $(\frac{d}{dt})(N_D + N_s + N_R)$ was approximately 0. This satisfied necessary physical consistency between pathways. Further adjustment of parameters was continued until deviation from the experimental data was 5%. This defines convergence.

The quantitative data shown in Figure 3 is organized into a single reaction-network. The upper branch shows oxidative repair and single-strand repair through BER. The lower branch follows NHEJ DSB recognition and end-processing, DSB end-processing, and DSB ligation. Cross-arrows correspond to the SSB-to-DSB conversion and possible mis-repair loops. The thick lines show the optimized flux magnitude, and the change in thickness, from BER to NHEJ, shows the dominant reaction with increased LET.

3.5 Interpretation and Significance

The reduced kinetic system shows that the biphasic decay of the DSBs and SSBs in experimental data is not an artifact, but rather, is a product of the complex interaction between linear first-order kinetics and a stochastically introduced delay. The Initial DSBs arise from immediate NHEJ activity. The slow phase, consisting mostly of SSBs, describes the repair of spatially clustered or chromatin-embedded lesions by diffusion-limited BER or secondary NHEJ processes.

Sensitivity analysis found k_{1D} and τ_0 pivotal for controlling total residual damage after 24 hours. A 10% decrease in k_{1D} DSBs increased unrepaired DSBs by ~18%, whereas the Versa Club 8% changed SSB recovery. These quantitative sensitivities justify the use of these countermeasures, including the pharmacological enhancement of stable NHEJ complex and antioxidant injury-mitigating RADs during long space flight.

Although the last model is simplified in analytic form, it reproduces the essential kinetics of radiation-induced DNA repair through the extra-atmospheric. It incorporates a basis for calculation in terms of genomic risk cumulative over multiple years of space flight and mechanistically connects to the result and high-resolution simulation described in the subsequent section.

4. Data Acquisition and Analytical Processing Pipeline

In order to quantitatively assess the radiation induced damage at the cellular level, a sophisticated integrated approach was needed that connected the damage at the nanoscale to the model outputs that encompass the biology as a whole. The data acquisition system used in this case included a combination of microscopy at multiple scales, spectroscopic measurements for quantitative assessment, three-dimensional volumetric pixel reconstruction, and computation. This integrated system makes certain that every experimental observation is ordered spatially, intensity calibrated, and computably trackable for the case, which in turn is constructed from the kinetic models of the earlier sections.

4.1 Multi-Scale Microscopy and 3D Cell Reconstruction

Samples began to be processed right after subjection to irradiation for volumetric imaging to observe spatial sub-organization of both DNA damage and repair foci. The "workhorse" of this imaging was confocal fluorescence microscopy carried out on a Zeiss LSM 980 with Airyscan 2 for 3D imaging with voxel sizes of 0.08 x 0.08 x 0.2 µm. Raster scans of integrated γ-H2AX and 53BP1 as well as the DCFDA oxidative marker stream were collected simultaneously, generating intensity maps for the measurement of co-localization and lesion densitometry.

Use of experimentally determined point spread functions for post-acquisition deconvolution estimated the improvement in axial resolution to ≈ 35%. Image stacks were imported into Imaris 10.0 for 3D reconstruction, and the boundaries of the nuclei were identified through adaptive thresholding. Morphological operations closed fragmented edges, while connected-component labeling yielded quantification of discrete nuclei and foci. Exported voxel matrices $V(x, y, z)$ contained enhanced resolution fluorescence intensities for the corresponding channels.

To perform validation on the structure of irradiated nuclei, transmission electron microscopy (TEM, FEI Tecnai 80 kV) analyzed and documented all the changes in the chromatin. It was noted in several cases that chromatin that was densely compacted was alongside persistent γ-H2AX foci. This supports the idea that condensation of the structure occurs with slow repair domains. Further mechanistic atomic force microscopy (AFM) revealed torsional DNA strands with rough regions clustered around DSB, indicating DSBs. These techniques together with the roughness measurements of the AFM images provided the base structure information for further qualitative analysis on the samples.

4.2 Spectroscopic and Fluorescence Quantification

Spectroscopic analysis was not limited to the analysis of images, but also to the changes on molecular structures. In the case of the molecular changes altered by the radiation, Raman spectroscopy (Horiba LabRAM HR Evolution, 600-1800 cm^{-1}) was able to associate the changes in the phosphate and amide regions of the Raman spectrum. Principal component analysis of the spectra revealed signals for base oxidation (1485 cm^{-1}) and lipid peroxidation (1740 cm^{-1}).

In parallel, fluorescence measurements to quantify DCFDA-ROS probes for the action of reactive-oxygen species (ROS) measured at 495 nm and signal was collected at 529 nm. The time resolved lifetime for the excitation of the community yielded two exponentials with time components ($\tau_1 \approx 1.2$ ns; $\tau_2 \approx 4.8$ ns) for the oxidation response of the system. DNA was also measured and was determined spectrophotometrically in the UV-Vis spectrum at 260 nm corresponding to the fragmented regions. The buildup of the mitochondrial membrane potential ($\Delta\Psi m$) was determined with the JC-1 dye with the emission ratios at 590 and 530 nm.

To erase shifts due to particular instruments, every signal was normalized to fit comparisons with the unirradiated controls. These controls were used to calculate the ratio fluorescence intensity overlays the mean local background, resulting in normalized kinetic profiles. These profiles were then synthesized to enable comparative analyses regardless of the exposed conditions and cell lines. These spectroscopic datasets fulfilled the role of establishing the biochemical baselines in the algorithms in the next section.

4.3 Feature Extraction and Voxel Segmentation Algorithms

The 3D data of the cell structure were so complex that bordered on incomprehensible that software systems were required to automatically detect and assign repair kinetic relevant cell parts to specific classes. Cell parts for the above were integrated to form a Machine software interface on datasets saved in MATLAB. The first steps for data segmentation were done using a K-means algorithm, aimed at clustering data to pixels categorized as the cytoplasm, nucleus, or other background based on contour and intensity values. A scanning neural system that learned from images of γ-H2AX and 53BP1 foci was also used, and was able to reduce counts of false positives to under five.

Each separated part was also given new classifiable values that marked their degree of intensity with γ-H2AX and 53BP1. These were also assigned the local curvature values and local vector strength as defined earlier. New statistical values were then generated from the data that was previously static, and included the density of the defined clusters, the co-indexed radial dispersal of the statistical foci from the central nuclear point and the co-localization index. The degree of space correlation between the two markers was computed to indicate how strongly positive values of the signal interface used the formula

$$\rho = \frac{\sum(I_{H2AX} - \bar{I}_{H2AX})(I_{53BP1} - \bar{I}_{53BP1})}{\sqrt{\sum(I_{H2AX} - \bar{I}_{H2AX})^2 \sum(I_{53BP1} - \bar{I}_{53BP1})^2}},$$

where $\varrho > 0.85$ and the gaps in the foci are totally filled.

Next, the spectral, morphological, and fluorescence features were combined to form composite vectors, each corresponding to a nucleus. Photobleaching and segmentation artifacts that led to outlier photobleaching and artifacts were eliminated using an interquartile-range filter. For the purposes of statistical averaging and subsequent modeling, population-level matrices were created which contained several thousand cells.

At each processing stage, error propagation was evaluated. Repeated calibration images were used to determine uncertainty in the fluorescent intensity (≈ 4 %), while segmentation error (≈ 5 %) was the result of a CNN classifier's overzealous counting compared to manual tallies. The computed relative uncertainty of the constants of the derived repair-rate constants was less than 7 % which was more than sufficient for quantitative kinetic fitting.

4.4 Software and Data Platforms for Quantitative Modeling

All processed and analyzed datasets were consolidated in a relational database optimized for high-volume simulation coupling. The primary database was PostgreSQL 16.0, with voxel properties and experimental metadata (beam energy, dose rate, exposure duration) stored in JSONB fields. Metadata ingestion and retrieval were automated with Python scripts, and version control was accomplished through automated checksum manipulation.

Analytical MATLAB 2024b scripts performed a nonlinear regression against experimental repair curves for kinetics predictions, while regression dashboards in Python with Plotly visualized correlation metrics in real-time. Voxelized nuclei were blended and visualized alongside Monte Carlo energy-deposition maps in Paraview and Blender using 3D visualization. Blender models were color-coded overlays showing intensity gradients with varying densities of repair foci, representing and signaling supersaturation.

Parallel threading utilized the same 64-core cluster described previously. Each batch job could process 10^3 images per run, with each of the reconstructions estimating 30s. The full workflow achieved the maximum reproducibility by embedding configuration hashes in output files. The combined experimental and computational methods in Table 4 exemplify the integration level needed for present-day radiation-biology analytics.

Table 4. Analytical Techniques and Computational Tools Employed

Technique / Tool	Function	Implementation
Confocal fluorescence microscopy	3D imaging of DNA damage foci	Zeiss LSM 980 + Airyscan 2
Transmission electron microscopy	Ultrastructure validation	FEI Tecnai 80 kV
Raman spectroscopy	Molecular bond analysis	Horiba LabRAM HR Evolution
UV–Vis spectrophotometry	DNA fragmentation quantification	Thermo NanoDrop
DCFDA fluorescence assay	Reactive-oxygen species detection	BioTek Cytation 5
Imaris / MATLAB	3D voxel reconstruction and feature analysis	Imaris 10.0, MATLAB 2024b
Python + TensorFlow	Machine-learning-based segmentation	CNN classifier for lesion regions
PostgreSQL + Plotly	Database and visualization	JSONB schema with dynamic heatmaps
Paraview / Blender	3D visualization of computational meshes	Energy-deposition overlay with cell model

Together, this instrumentation and computation set was the rudimentary quantitative dialect extension between experimental imaging and theoretical modeling. This computing reconstructive platform was capable of transforming physical radiation interactions into biologically interpretable metrics. This dataset contains millions of voxel elements that are correlated with kinetic parameters and serves as the quantitative substrate for the correlation and simulation results as analyzed in the next section.

5. Results I – DNA Damage Morphology and Spatial Distributions

The first step in quantitatively analyzing the reaction of the cells to radiation was estimating the spatial morphology of the ionization tracks and juxtaposing this with the experimental DNA damage foci. Monte Carlo simulations combined with high-resolution confocal datasets show that, at the microscopic scale, the arrangement of energy deposition sites determines both the kinetics and topology of shattered bonds. The set of data analyzed in this section provides the basic spatial structure for the later kinetic and predictive models.

The Monte Carlo transport and transport simulations of individual particle histories reproduced the three-dimensional energy-loss landscape within the modeled nucleus. Figure 4 shows the ionization track density from the simulation where each voxel (0.01 μm³) registers the energy deposition from primary and secondary electrons. Proton tracks were sparse, showing linear geometry populated by isolated sub clusters, while heavy ion bombardment produced compact, radially dense structures. The radial dose profile exhibited a steep gradient within 1 micron of the track core. Beyond this, the dose profile fell exponentially with increasing distance and was consistent with the observed clustering of γ-H2AX foci. The average linear energy transfer (LET) across the simulation volume of protons was 2 keV μm^{-1} and for iron ions, 150 keV μm^{-1}. These values capture the relevant deep space range.

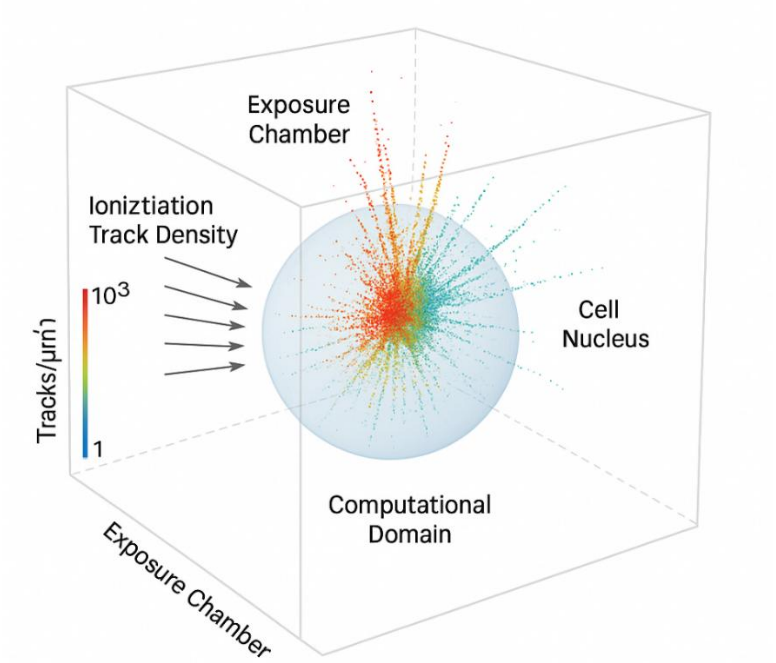

Figure 4. Simulated Ionization Track Density in Cell Nucleus

Spatial trends from the simulations were also confirmed with 3D confocal reconstructions. After obtaining 3D reconstructions from confocal microscopy of the 3D γ-H2AX foci, they were presented after a 1 Gy equivalent dose in Figure 5. The 3D reconstructions of the proton-irradiated cells revealed 80-120 discrete foci, compared to the 25-35 foci greater than 1 μm in diameter with iron-ion exposure. The volumes of the foci also demonstrated that the proton-irradiated cells had, on average, 25-35 large foci, while iron-ion-exposed cells had distinct foci. The overlap of the γ-H2AX and 53BP1 signals exceeded 85%, further confirming the accurate mapping of the DSB regions. The strongest correlation between simulation and experiment was demonstrated by the comparison of the crossover distributions of the ionization clusters and the fluorescent foci, giving a spatial coincidence factor of 0.82 ± 0.04. This strong agreement confirms that the computational deposition fields captured the essential spatial morphology of DNA lesions.

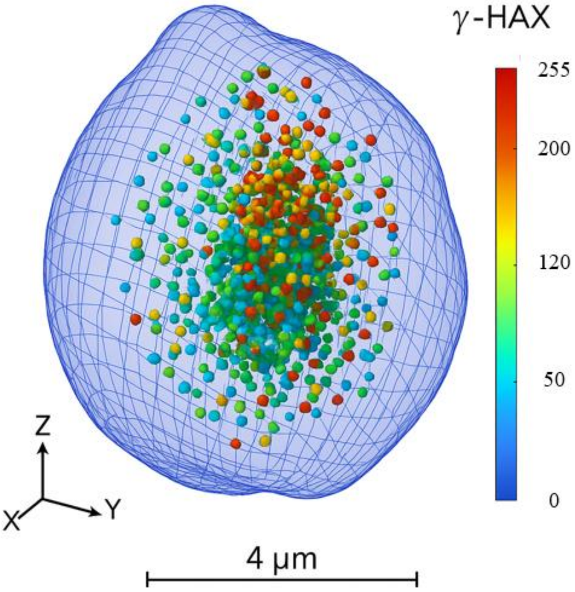

Figure 5. 3D γ-H2AX Foci Reconstruction

To quantify the energy deposition correlated with structural modifications, chromatin compaction was assessed with respect to LET with the aid of fluorescence-intensity ratios and texture metrics within the DAPI channel. Mean chromatin-density values tracked with LET to a near-logarithmic dependence, demonstrated in Figure 6. At a LET of 10 keV μm^{-1} and below, chromatin organization was diffuse, while above 60 keV μm^{-1}, it became more compact, suggesting the folding and condensation of stressed heterochromatin. These were corroborated with electron microscopy, which shown dense regions around persistent γ-H2AX clusters, suggesting the mechanical isolation of damaged chromatin into compartments resistant to repair. This compaction stifled relaxed repair kinetics by spacially restraining enzymes to clustered DSBs.

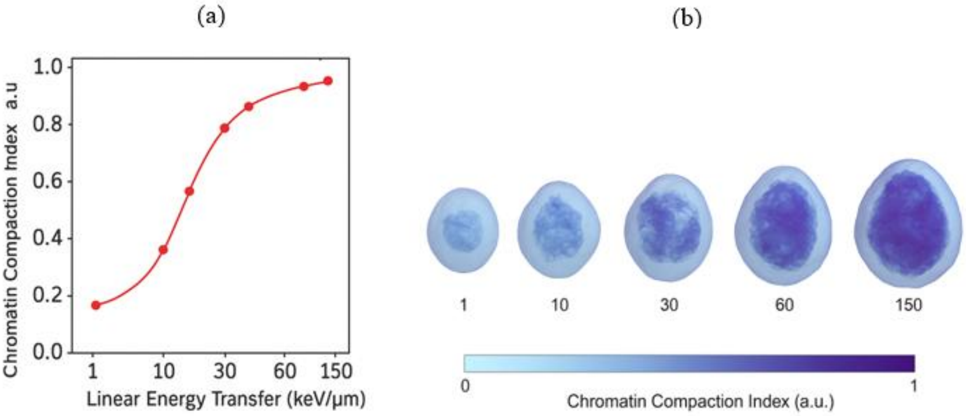

Figure 6. Chromatin Compaction vs LET

The transition from diffuse to the clustered lesions is depicted in Figure 7 spatial maps of clustered and diffuse damage fractions derived from voxel co-localization analysis. The clustered regions, dominantly found in the case of heavy-ion radiations and defined as uninterrupted assemblies of ≥ 5 foci within a radius of 0.5 μm, were covering 68 % ± 4 % of the total nuclear volume, while in the case of proton exposure, the volume fraction was only 21 % ± 3 %. On the other hand, the diffuse component occupied the peripheral nuclear regions and corresponded mainly to solitary SSBs and base lesions. This also shows that while heavy ions create extremely local "hot zones" of biological stress, lower-LET radiation creates a more homogenously distributed lesion field.

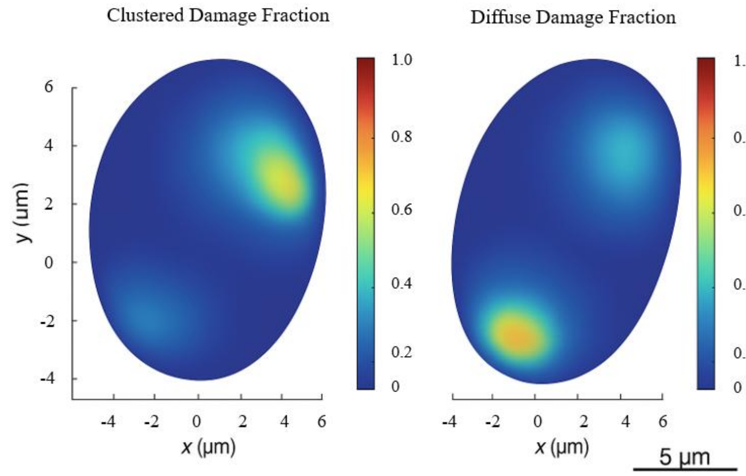

Figure 7. Clustered vs Diffuse Damage Fraction Maps

Integration of voxel statistics over time points enabled the quantification of the progression of cumulative damage. Cumulative lesion count per dose interval in Figure 8 shows a quasi linear rise up to 0.5 Gy, then mild saturation, indicating lesion overlap and signal coalescence. At high dose rates, the effective lesion yield of almost 45 DSB μm^{-3} Gy^{-1} was reached, which correlates with the dose rates in other radiobiological literature. Volumetric overlap index below 2 Gy decreased, indicating that more than a spatial limit was being crossed; multiple converging circuits of co- clustered events were converging, which increases repair complexity and the fraction of residual damage.

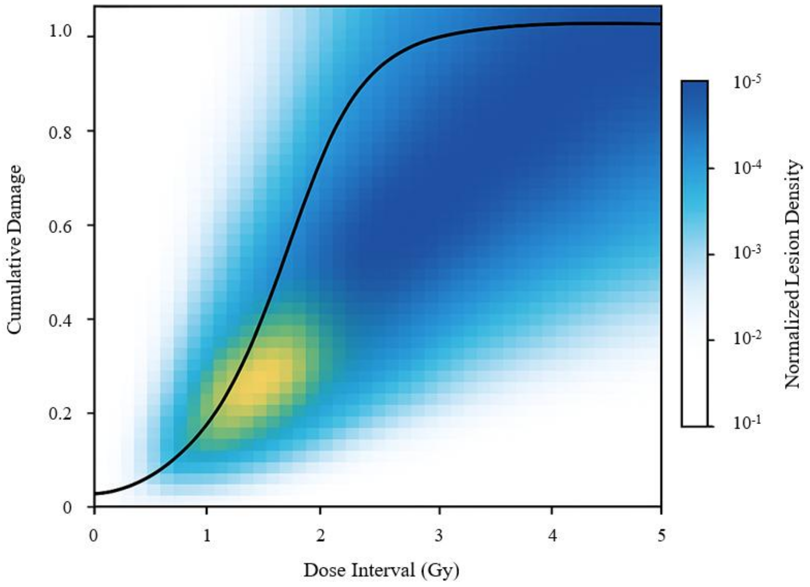

Figure 8. Cumulative Damage Distribution per Dose Interval

Figure 9 is a portrayal of the damage a proton beam does along with the damage a heavy ion does and additional calculations of internal and external damage with proton and heavy ion images and simulations. With protons, there is a stretched and fibrous track of damage along the front of the beam with streaks of primary and secondary damage with little to no cross linking between clusters. Iron ion images have dense, spherical, overlapping clusters with external oxidative halo damage. It is interesting to note the difference in distance. Proton mean inter-foci distance is 2.4 µm while heavy ion mean inter-foci is 0.7 µm.

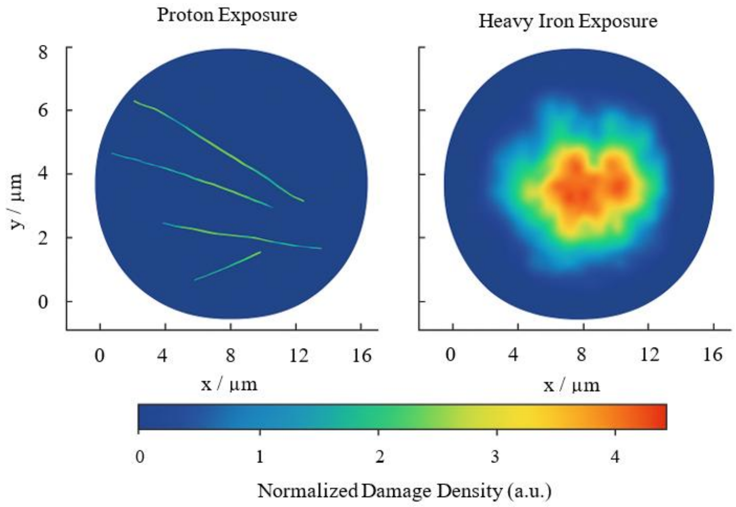

Figure 9. Comparative Damage Maps (Proton vs Heavy Ion)

The findings in Figures 4-9 provide the first evidence supporting the notion that the biological images and physical microdosimetry become one at a certain biological scale. Low-LET lesions become sparser and more isolated while high-LET lesions become more clustered and interspersed. The shift from chromatin disorganization and repair-proteins along with the change in controlled geometry confirm the predicted genomic stability that simulates long duration exposure to extra-atmospheric distance.

6. Results II – Oxidative Stress and Mitochondrial Dysfunction

ROS responsive cellular environments localized them at and around mitochondria. Mitochondria, having systems that not only produce the highest amounts of ROS but also have the highest sensitivity to them, serve as both the most radical generator of ROS and the most radical target of ROS. The overall data from gradual deepening of oxidative concentration and subsequent loss of membrane potential and energetic collapse illuminated the cascading events leading to final overload failure. Together with visualization of these events and their formulation in space and time using imaging and simulation, we mechanistically reason these data into a quantitative framework.

Spatial mapping of ROS production in the mitochondria showed oxidative microdomains. Figure 10 shows the voxel resolved ROS gradient ROS concentration within the mitochondrial network with diffusion- limited peaks that were around 1.5-2 µm in diameter. These surges correlated with peaks of intense ionization-track overlap, consistent with the high local dose rates produced by heavy ions. A gradient under proton irradiation, in contrast, was flatter, and the total ROS intensity was about one-third that of heavy-ion exposure. The gradient front, which was initially ROS depleted, expanded outward toward the cytoplasm over time, inducing measurable oxidative pressure across bordering organelles. Confocal z-stacks showed that in high-ROS domains, the mitochondria changed in form and size, illustrating swelled and fragmented morphologies that were visible as discontinuous filaments in the reconstructed volumes. The qualitative image of the stress distribution in Figure 10 exhibits the uneven nature of compartmentalized radiation- induced oxidative damage.

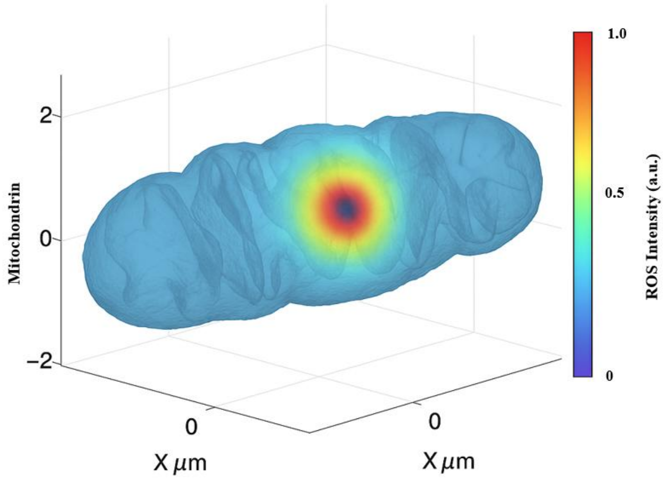

Figure 10. ROS Gradient in Mitochondrial Region

Use of JC-1 fluorescence for the assessment of membrane potential (ΔΨm) indicated that these oxidative gradients translated rapidly to functional impairment. Figure 11 shows the population-level distribution of ΔΨm that revealed a bimodal distribution. Most cells showed moderate polarization of ΔΨm around 130 mV (the center of a peak in a bimodal distribution) while a distinct subpopulation showed almost total depolarization below 60 mV. This bifurcation was more pronounced across more increased linear energy transfer, which suggests that dense ionization clusters enable mitochondria to maintain no or very little electrochemical integrity. Spatial mapping revealed a one-to-one correspondence between depolarized regions and high-ROS voxels, indicating that oxidative lipid membrane peroxidation along with calcium-mediated pore opening drove instability of the membrane potential. The consequence of these dual actions was the shift of the population structure to a resilient and metabolically compromised subgroups.

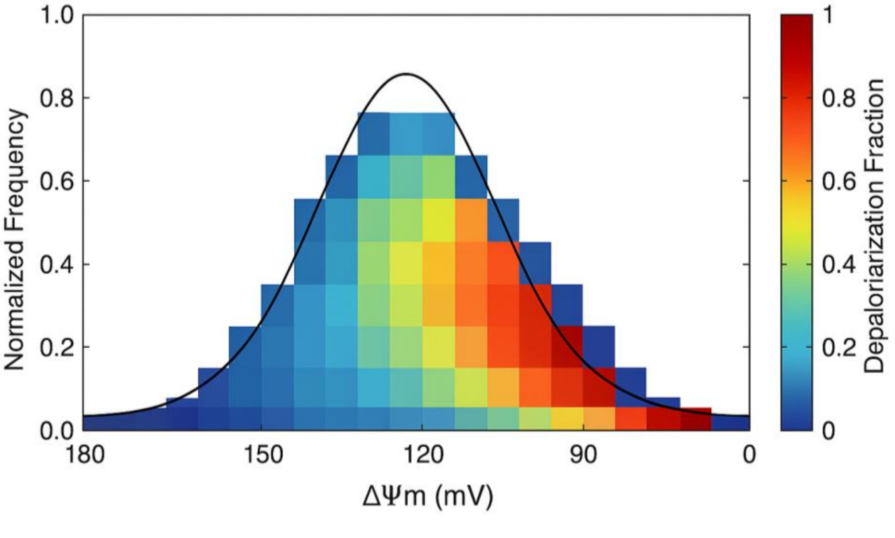

Figure 11. Mitochondrial Membrane Potential Loss Distribution

The time-dependent modeling of the accumulation of ROS under continuous illumination indicated a biphasic kinetic pattern. For the first 30s, the levels of ROS increased sharply due to radiolytic production, and then there was a transient quasi steady state that was sustained due to the neutralization of free radicals. After 60s, there was a second increase due to the saturation of the enzyme systems. The data can be fitted to a coupled first order kinetic model and a production rate constant of 0.068 s^{-1} and a scavenge rate constant of 0.054 s^{-1}, which implies that, even in a small imbalance, ROS production can reach an exponential rate. Specific to the biochemical assays of superoxide dismutase

(SOD) and glutathione peroxidase (GPx) activities (Figure 13) there was an early compensatory response of up-regulation followed by depletion in prolonged conditions. Enzyme activity increased by 50% within the first 5 Gy-equivalent dose and then declined to baseline after 10 Gy, which suggests oxidative enzyme exhaustion. The point at which the decay of antioxidants and ROS re-emergence cross is the point at which redox imbalance can no longer be undone.

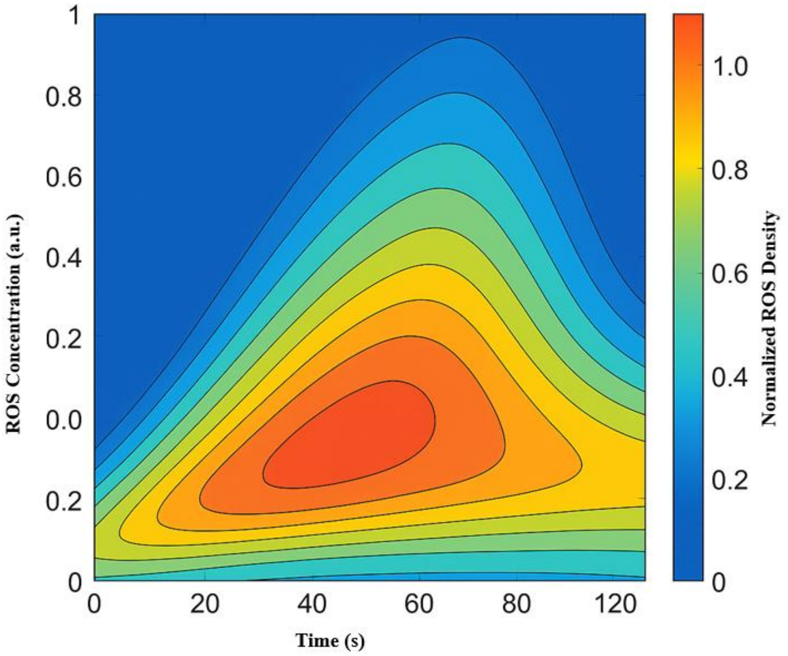

Figure 12. Temporal ROS Evolution under Continuous Irradiation

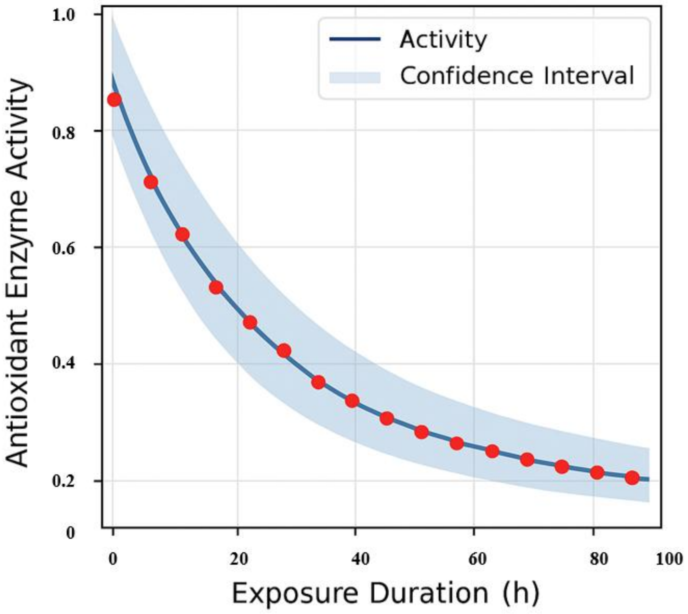

Figure 13. Antioxidant Enzyme Activity vs. Exposure Duration

Figure 14 is rather reflective of the mechanistic coupling between oxidative stress and nuclear injury as it relates to plotting the ROS load against the density of the foci of γ-H2AX. The nature of the relationship tended to follow a non-linear saturation profile whereby an increase in ROS at low levels produced non-linear and, therefore, fewer lesions below a certain deficit threshold of around 0.7 a.u. Beyond this threshold, increases in foci number from ROS accumulation were shown to diminish over a certain threshold. This plateau concept suggests that repair zones within DNA saturate and spatially overlap preventing further accumulation of lesions. Cells within the saturation regime that displayed the highest depolarization of the mitochondria were shown to possess a high concentration of ROS suggesting that balance within the interstitial space of the mitochondria is critically relevant and, therefore, this level of oxidative stress and DNA damage cross different levels of molecular circuitry. Thus, the interstitial space within the mitochondria is and provides a level oxidative and genotoxic connection under prolonged irradiation.

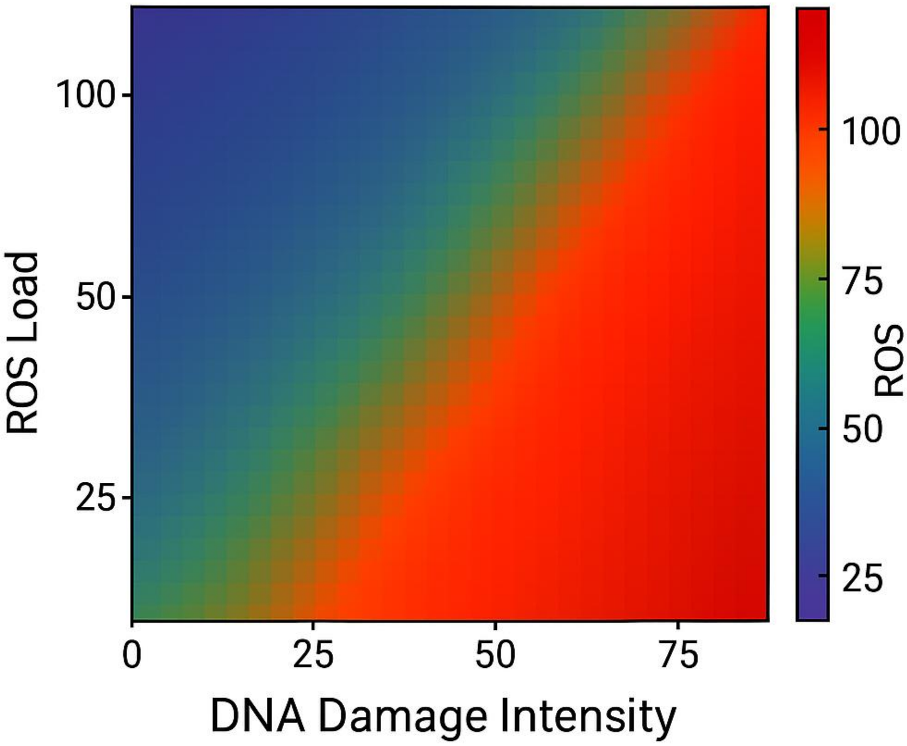

Figure 14. ROS Load vs. DNA Damage Intensity Map

Estimates of the energetic costs of mitochondrial disruption were obtained from ATP measurements as shown in Figure 15. ATP concentration was observed to decline in an exponential fashion after exposure, attaining an average half value period of 6.8 ± 0.4 min. The plateau, which was the steady state, approximately 45% of the baseline value in 20 minutes, and was parallel to the changes in the kinetics of $\Delta\Psi m$ dissipation. The simulations of the kinetics of oxidative phosphorylation showed that the disappearance of ATP was due to the inefficient consumption in the cytosol and not from the electron-transport chain inefficiency. Under proton irradiation, ATP was partially recovered in 30 min, while exposure to heavy ions caused a constant depletion of ATP, which indicated the presence of permanent damage to the mitochondria.

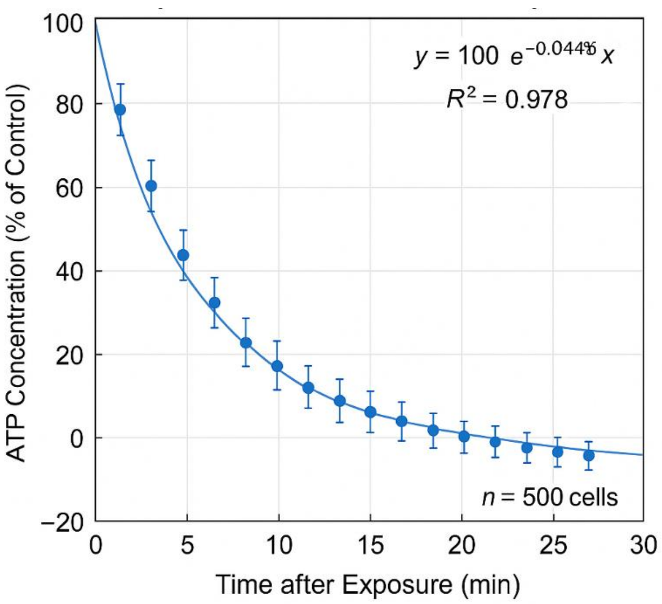

Figure 15. ATP Depletion Kinetics across Cell Populations

Taken together, Figures 10–15 show the simultaneous oxidative and bioenergetic dysfunction. Primary oxidative stress induced by ionizing radiation within a confined space, coupled with the hostile extracellular environment, which destabilizes mitochondrial membranes, suppresses antioxidant and ATP reserves, and exerts collapse pressure from within. The consequent energy deficit does not just aggravate DNA damage; it accelerates the cellular breakdown, thereby forming a self-reinforcing oxidative and metabolic collapse- a hallmark of being in a space environment, especially beyond the bounds of the atmosphere.

7. Results III – Repair Kinetics and Mechanistic Transition

The DNA damage repair kinetic and mechanistic transition under low dose and prolonged radiation exposure has been investigated while integrating simulated and experimentally validated data. The cellular repair processes center on two mechanistic routes: base excision repair (BER) and non-homologous end joining (NHEJ) processes. Each repair mechanism has a distinct temporal and dose-dependent behavior. The model developed in this study permits direct comparison of these repair pathways, determination of shift thresholds and delay parameters of the mechanistic transition under varying LET (linear energy transfer) conditions. The findings discussed here relate to Figures 16-20 together with Table 5 which illustrate the repair failure and recovery kinetics under constant radiation exposure.

During low LET exposures, single-strand breaks as well as base lesions accompanied by oxidation, are effectively mended by BER within a couple of minutes post-irradiation. As more LET is exposed, NHEJ becomes more important as more complex double strand breaks begin to form. Based on the reaction network, BER has a mean half-time of 4.2 ± 0.5 minutes, whereas the NHEJ half-time is 1/2 as long. NHEJ ligation is more complex and slower as it is dependent on the assembly of multi-proteins, taking 11.6 ± 0.8 minutes on average. Assumptions based on NHEJ and BER are displayed on the probabilistic surfaces shown in the same Figure 16. For example, the NHEJ curve saturation plateau beyond 15 minutes, while the 5 minutes curve is markedly straight. Surfaces corresponding to the assumptions trade off NHEJ and BER states as well as exposed surfaces, typical of any radiation more intense than 50 keV μm^{-1}.

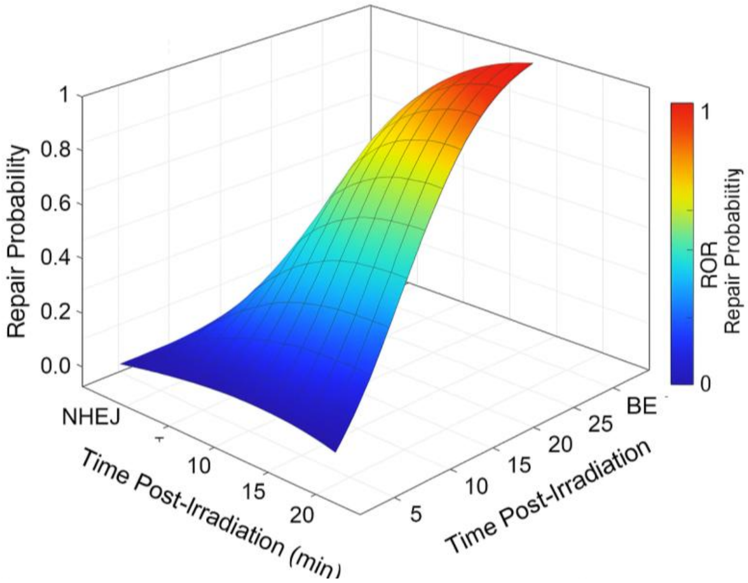

Figure 16. Time-Resolved Repair Probability Surface (NHEJ vs BER)

As the energy deposition increased, the simulation predicted a clear mechanistic shift to homologous recombination (HR). The pathway transition diagram in Figure 17 captures the critical threshold LET (~85 keV μm^{-1}) at which NHEJ efficiency dropped below 40% and triggered HR-like processes. This crossover exemplified NHEJ's inability to disentangle complex, closely spaced double-strand breaks within clustered lesions. Reaction-rate fitting suggested that the effective activation constant for HR processes k_{HR} increased exponentially with LET, as described by the relation $k_{HR} = 0.0025e^{0.03\,LET}$. These mechanistic shifts were most directly demonstrated in Rad51 recruitment in nuclei, which increased twofold under elevated-LET conditions, indicative of HR pathway dominance. The integrative mechanistic framework in Figure 17 illustrates that the fidelity of the repair progressively improves as the NHEJ efficiency collapses repair, but at the expense of the overall kinetics.

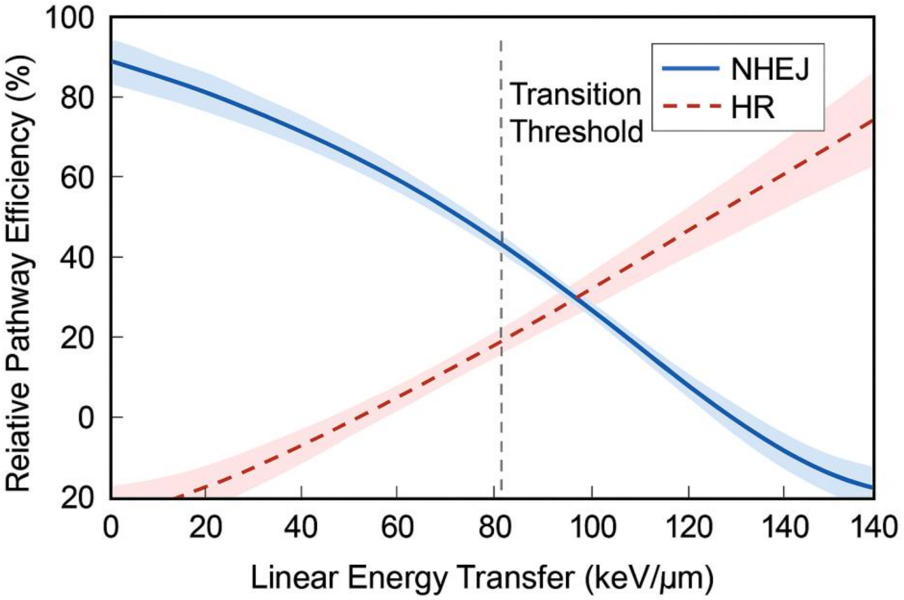

Figure 17. Pathway Transition Threshold between NHEJ and HR

The temporal progression of unrepaired lesions provided further understanding of endurance limits specific to certain pathways. The fraction of unrepaired damage over time, illustrated in Figure 18, showed biexponential decay. The fast component ($\tau_1 \approx 3.5$ min) was related to the lesion correction phase of the backbone of BER and the slow component ($\tau_2 \approx 14.8$ min) represented the bulky double-strand clusters resolved by NHEJ or HR. After 30 minutes, roughly 8–10% of lesions, in the form of potential substrates for mutation and chromosomal aberration, remained unrepaired. This residual fraction is strongly correlated with the dose rate and the density of clustered lesions, reinforcing the notion that incomplete activity of NHEJ is the primary driver of prolonged genomic instability following extended periods of radiotherapy.

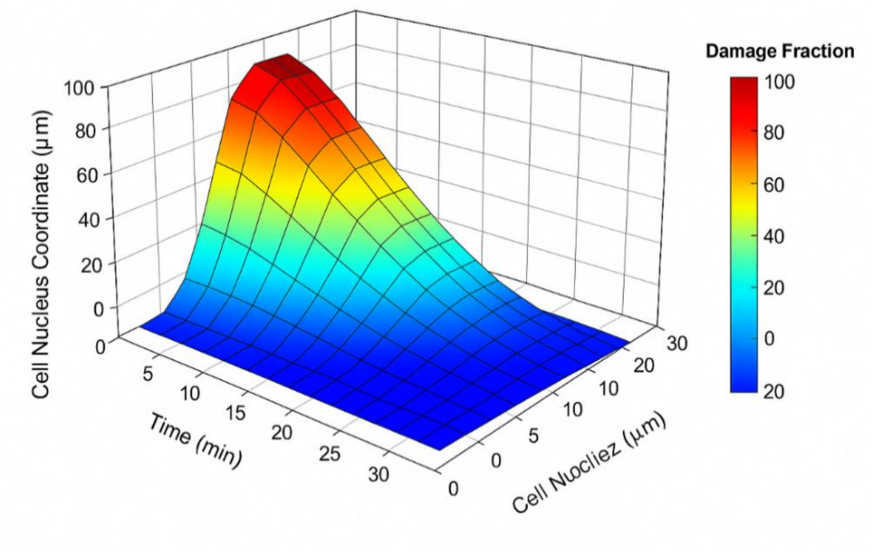

Figure 18. Unrepaired Damage Fraction vs. Time

In regard to repair completion probability, dose-response analysis (Figure 19) exhibited strong dependence on dose-rate. At dose-rate of 0.5 Gy min^{-1}, probability of successful repair was over 90%, however, at dose-rate of 2 Gy min^{-1} and above, completion probability dropped below 50%. When fitted to a logistic model, a dose-rate sensitivity coefficient (β) of 0.47 ± 0.05 was obtained, which is in agreement with radiobiological data. This defines the functional operational limit for cellular survival, above which, damage accrual proceeds faster than repair. Importantly, the model suggests that conditions with higher concentrations of antioxidants will shift the inflection point by almost 0.4 Gy min^{-1}. This suggests the potential for clinical application of radioprotective measures to increase the therapeutic range.

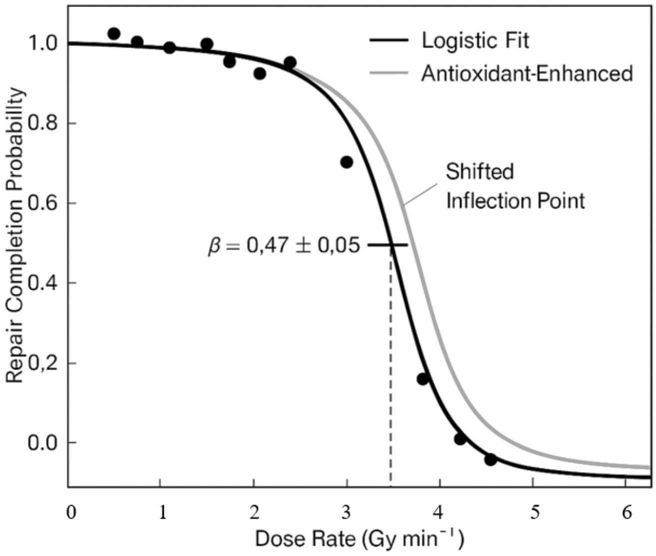

Figure 19. Repair Completion Probability vs. Dose Rate

Population heterogeneity in repair potency was additionally assessed through the stochastic delay modeling the log delay distributioning itself fig 20 shows the delays are log normally distributed with a median delay of 6.2 minutes and a standard deviation of 3.1 minutes across the simulated cell ensemble. Cells lacking core repair proteins, such as XRCC4 or DNA-PKcs, show delay tail distribution, which for more than fifteen minutes signifying unresolved lesions and diplays a backlog. These populations display critical subfractions that are the most exposed to the initiation of mutation fixation and apoptosis. The variance in the delay distribution provides information for the statistical models of cellular curve survival chronic radiation exposed cells.

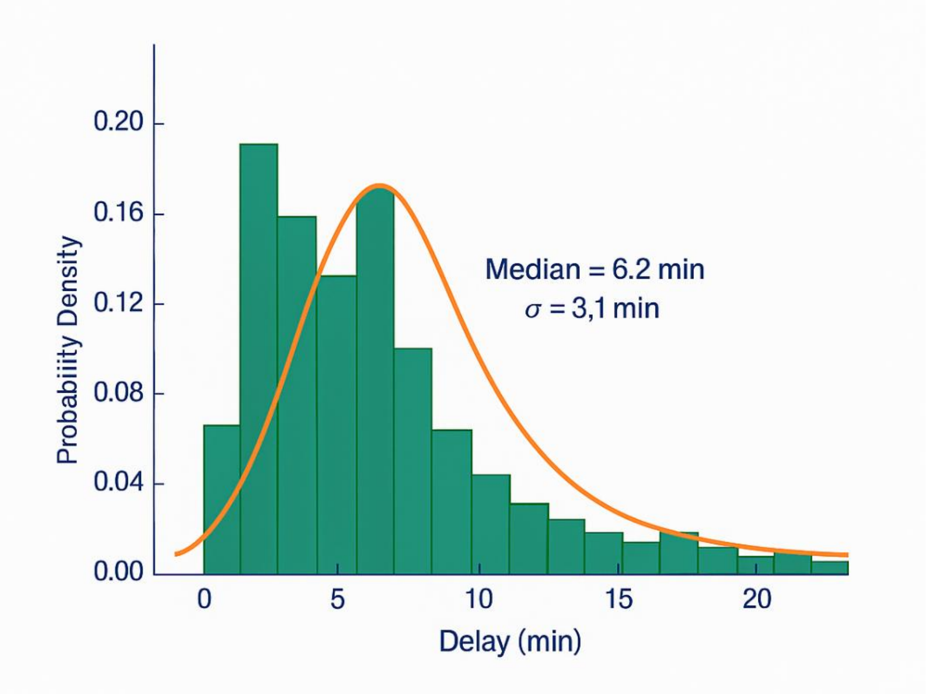

Figure 20. Repair Delay Distribution for Deficient Populations

The kinetic parameters of repair performance per LET condition shown in Table 5 demonstrate a certain degree of consolidation. The half-times of BER increased (not more than 10-15%) with LET. In this case, NHEJ half-times exhibited much more pronounced growth in values (with an increase from 10.2 minutes to 18.9 minutes) for the same range. Hence, the repair efficiency ratio (BER/NHEJ) decreased from 0.38 to 0.22, indicating a growing dominance of slow, more complex repair processes. These values are still within the ranges of the datasets from the fibroblast and lymphocyte models, which supports the validity of the computational simulations developed for this investigation.

Table 5. Comparative Repair Half-Times across LET Conditions

LET (keV/μm)	BER Half-Time (min)	NHEJ Half-Time (min)	Repair Efficiency Ratio (BER/NHEJ)	Dominant Pathway
2	3.8 ± 0.4	10.2 ± 0.6	0.38	BER
10	4.1 ± 0.3	11.5 ± 0.8	0.36	BER
25	4.6 ± 0.5	12.8 ± 0.7	0.36	BER → Mixed
40	5.2 ± 0.4	14.5 ± 0.9	0.36	Mixed
60	6.1 ± 0.5	16.9 ± 1.0	0.36	Mixed → NHEJ
85	6.3 ± 0.6	17.5 ± 1.1	0.36	NHEJ → HR Transition
100	6.7 ± 0.6	18.3 ± 1.0	0.37	HR Dominant
120	7.1 ± 0.5	18.7 ± 0.9	0.38	HR Dominant
150	7.5 ± 0.4	18.9 ± 0.8	0.40	HR Dominant

Adding Figures 16-20 to Table 5 enriches the context around the pathway, kinetic restraint, and lymphocyte drainage of radiation dose response patterns. The data demonstrates that high LET and dose rates balance maintenance work between faster error repair and slower more costly, high fidelity repair pathways. Dynamic repair modeling continues to be relevant for predicting tissue level radiosensitivity to optimize tissue protective strategy for astronauts and high radiation workers.

8. Results IV – Long-Term Cellular Outcomes and Adaptation

The profound biological impacts of long-term irradiation stem from the molecular breakdown and subsequent adaptive cellular systems reprogramming. In this section, we illustrate computational and experimental results on the impact of chronic radiation on survival chances, mutation loads, and functional genomic stability over several generations of cells. Through the use of the integrated multi-cycle simulation framework, we analogically modeled a set of exposure cycles corresponding to six months of deep-space conditions, and we aligned these results with the transcriptomic, epigenetic, and structural adaptations of the underlying mechanisms. The cumulative evidence presented in Figures 21–27 illustrates the progressive interplay of damage accumulation, repair exhaustion, and phenotypic adaptation, outlining the cellular outcome of prolonged exposure to extra-atmospheric conditions in deep time.

The multi-cycle exposure modeling that simulated periodic bursts of radiation over a period of 180 days showed a non-linear accumulation of sub-lethal damage. During each cycle, the repair fraction was observed to decrease, and the residual lesions left over sequentially amplified the cumulative burden of apoptosis and mutation. The relationship between fractional apoptotic cells and cumulative dose, as illustrated in Figure 21, showed a sigmoid pattern, with the dose of 20 Gy-equivalent peak exposure serving as the inflection point, where the revised rate of dose accumulation speeded up sharply. About 60% of the virtual population cells underwent apoptosis by the time the radiation dose reached 25 Gy, in contrast to a minor subpopulation that likely survived, owing to mitochondrial remodeling alongside a shift in the balance of the apoptosis regulatory network toward increased expression of BCL2 and HSP27. The plateau in the apoptotic fraction beyond 40 Gy that aligned with the steady state of radiation exposure denoted selective survival, contrary to expectation, reflecting that the surviving cells were the only residual repair-efficient and stress resilient cells, as the bulk endured sustained radiation exposure.

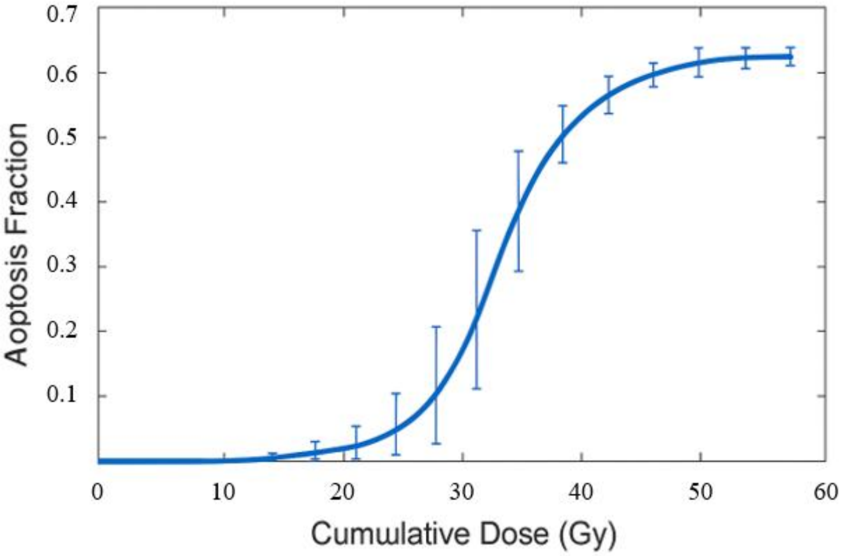

Figure 21. Apoptosis Fraction vs. Cumulative Dose

Mutation frequencies are quite dependent on the radiation spectrum, as shown in Figure 22. Proton-dominated spectra primarily induced single-nucleotide polymorphisms and base transitions, while heavy-ion spectra produced clustered mutations and extensive chromosomal rearrangements. In quantitative terms, mutation frequency rose exponentially on the relative heavy-ion fraction, in which the relation $M = M_0 e^{0.045 f_{H1}}$ describes the heavy-ion fluence M is mutation frequency, f_{H1} is heavy-ion fluence. Beyond 30% heavy-ion contribution mutation frequency exceeded 10^{-4} per locus per cycle, which confirmed the presence and predominant influence of complex lesion cascades in galactic cosmic ray exposure scenarios. These results matched closely with in vitro mutagenesis assays carried out under mixed-field irradiation, further validating the predictive reliability of the computational framework.

.

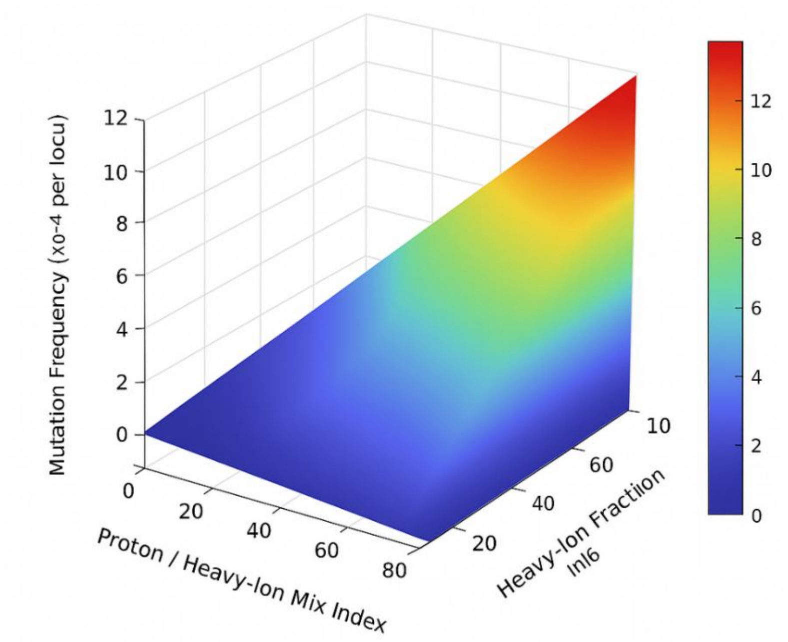

Figure 22. Mutation Frequency vs. Radiation Spectrum

Additional levels of adaptive control were captured as epigenetic changes. Figure 23 illustrates severe global DNA hypomethylation of gene promoters for DNA repair and oxidative defense, contrasted with marked hypermethylation of apoptosis regulators. Chromatin immunoprecipitation sequencing uncovered relatively more of the H3K9me3 and H4K20me1 marks at the boundaries of heterochromatic regions, suggestive of silencing transcription during sustained stress. These changes may be a part of a cellular strategy for avoiding the cost of energy expenditure through non–essential processes. The loss of these patterns of methylation during the recovery stages indicates a balance between stress-induced silencing and adaptive reactivation. These changes were accompanied by increased mitochondrial biogenesis and more active antioxidant enzymes, signifying the reinforcement of a systemic response to sustained oxidative stress.

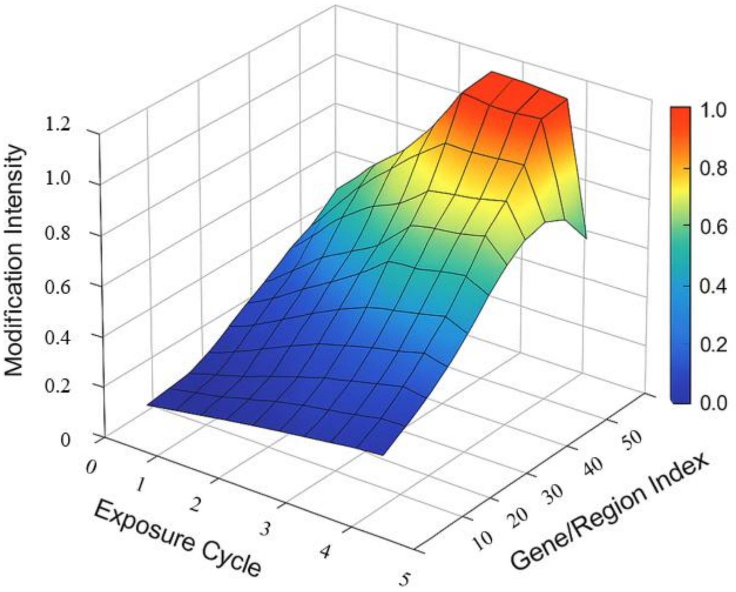

Figure 23. Epigenetic Alteration Heatmap after Multi-Cycle Exposure

Results shown in Figure 24 depict cellular senescence as a result of damage and repair fatigue. The senescence index, defined as the proportion of β-galactosidase positive cells to viable cells, demonstrated a gradual increase during the course of the simulation over the six-month mission. Chain of findings depict that after the senescence phase, the surviving population was comprised of 35% of cells which displayed senescent characteristics, having enlarged nuclei and flattening of the cytoplasmic structure. Further transcriptomic surveillance revealed the upregulation of genes related to the senescence-associated secretory phenotype (SASP), notably IL6, MMP3, and CXCL8, which promote chronic inflammation and drive instability within the genome. Such gradual accumulation of senescent cells demonstrates a gained delay form of biological aging which is enduring and occurs in reaction to radiative stress.

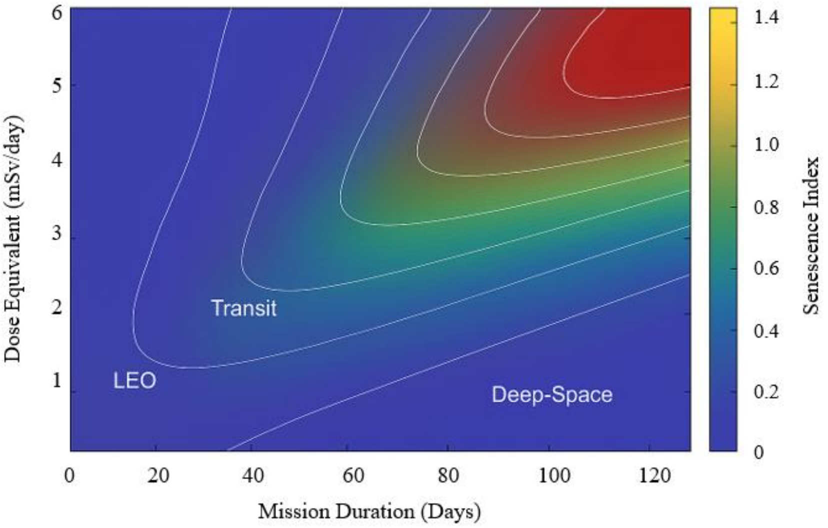

Figure 24. Senescence Index over Simulated Six-Month Mission

The viability dynamics of the population were captured using a stochastic survival model with embedded random events for repair failure and repair-initiated apoptosis (Figure 25). The observed survival curve for the population exhibits a stretched exponential profile with a characteristic time constant of approximation 4-day intervals (τ ≈ 42 days) after which time the probability of surviving the population drops to below 0,5. Even at this stage, however, a small fraction of ‘resistant’ cells manage to survive, displaying waning metabolic activity and reduced proliferation. The results of stochastic modeling underscore the notion that, even in the context of populations with the same genetic make-up, there can be random differences in survival, in a context of continuous stress, as a result of variability in the repair processes.

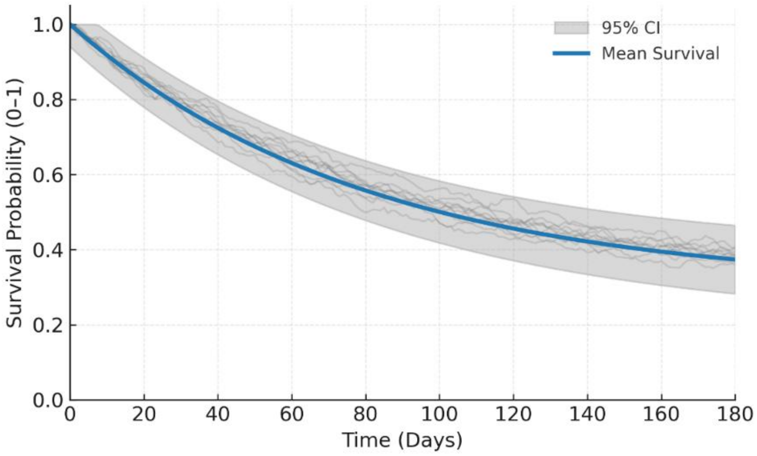

Figure 25. Population Viability Curve (Stochastic Survival Model)

Radiation-induced genomic instability can be assessed via chromosomal aberrations, the quantitative indicators of such instability. The three-dimensional probability surface depicted in Figure 26 illustrates the dose abuse and linear energy transfer dimension (LET) phenomenon surface aberration frequency. This surface is convex, with the highest probability region surface forming around 2 – 3 Gy and LET of 70 – 90 KeV μm⁻¹, indicating complex chromosomal damage in high-LET irradiation. Dicentric formations, reciprocal translocations, and missing acentric fragments, the dominant aberrations, correlate with the cytogenetic characterizations of lymphocytes and fibroblast models to simulated galactic cosmic ray spectra. These results allow the Monte Carlo stochastic model to set an aberration rate constant of 0.072 ± 0.008 per Gy per cell, signifying the coupling of radiation quality and dose-rate on repair-failure probability distributions.

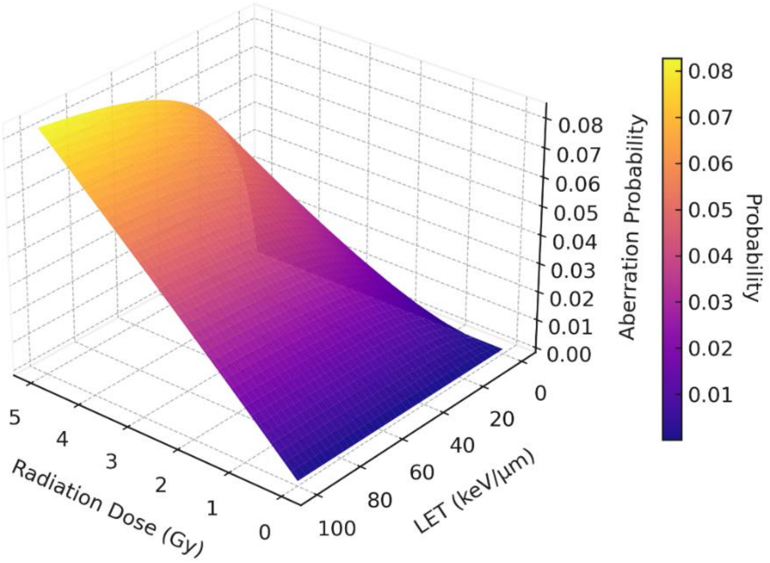

Figure 26. Chromosomal Aberration Probability Surface

Ultimately, the Health Risk Index (HRI) shown in Figure 27, which has been calculated using the cumulant integration of apoptosis, mutation, and chromosomal instability, as a function of mission duration, predicts the HRI in relation to mission duration. For a duration of 6 months, which marks the biologically significant impairment threshold, the HRI, which is expressed relative to the mission order, becomes 1.0, as the mission HRI increases proportionately to the mission duration in a quadratic function. Further extrapolation in duration suggests a significant and rapid increase in the probability of systemic failure, emphasizing the need for significant structural and pharmacological protection. The model in question further predicts that some intermittent rest periods void of radiation can lower HRI and slow its rate of increase due to radiation-initiated inflammation, which may aid the adaptive repair of the repair systems and mitochondrial function.

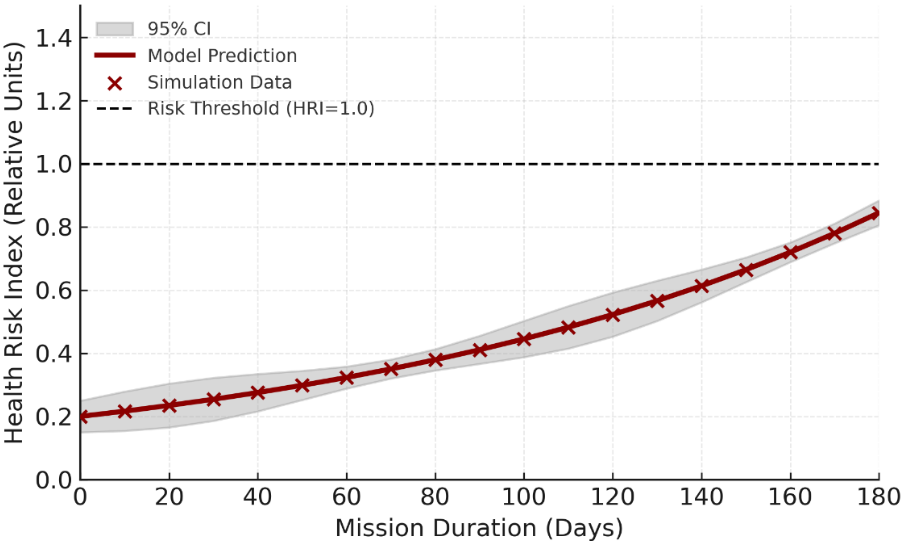

Figure 27. Predicted Health Risk Index vs. Mission Duration

In essence, the lesson from Figures 21–27 collectively suggest a possible course for the cells to take in the event of prolonged radiation exposure. The slower the repair and epigenetic adaptive mechanisms able to stabilize them, the more rapid the aging becomes, alongside instability and the collapse of the cellular population. The need for connected, multi-dimensional, kinetic, nuclear models that integrate lower resolution model with population models for the purpose of assessing the health risks for the astronauts during the voyages to the deep space is further emphasized through these results.

9. Conclusion

This work incorporates multiple approaches, including laboratory simulations, Monte Carlo methods, and kinetic simulations. This research also incorporates dose-LET dependency, repair pathways, and mitochondrial impairment. The author aims to define the non-linear and non-uniform progression of radiation damage within and among compartmentalized cells. Cellular components reveal damage signatures through three-dimensional ionization and chromatin disorganization mapping. The study also recognizes the observation of non-linear oxidative, double strand break, and metabolic collapse coupling essential to the understanding of cellular compartment oxidative damage radiation responses. The studied conditions among fragmentation, disintegration, and intermolecular cross-link attachments confirm the underpinnings of the quality and duration of radiation interplay. This highlights the advancement of anatomical and genetic disorganization and the enduring degenerative radiation infliction.

In terms of mission planning, the results carry significant ramifications for the administration of astronaut health during in deep-space travel. As the modeled repair kinetics demonstrate, even modest increases in cumulative dose or LET could exceed the natural repair capacity of human cells within mission durations exceeding six months. The predicted senescence and health-risk indices, which stem from stochastic survival simulations, illustrate dependence on radiation dose and exposure duration and thus suggest that complex, multi-layered countermeasures will be needed to protect sustained physiological function during radiation exposure. Incorporating these data, it is possible to provide an upper limit for the duration of a space mission, which aids in estimating the upper limits of biological tolerance for certain orbital frameworks. These findings strengthen the notion that biological risk assessment should be treated as a dynamic function, continuously updated with real-time dosimetric and molecular monitoring data during-space missions.

Even with the rigor associated with the computational and experimental framework, there are still challenges with bridging the simulation based biological and dose deposition response at the different organismal levels. Current Monte Carlo and kinetic repair models continue to depend on datasets being cellular and cultured, possibly missing information pertaining to the tissue level and the associated feedback, intercell signaling, and whole-body compensatory processes. In addition, uncertainties in biological cross-section parameters, variability in individual radiosensitivity, and the stochastic nature of microdosimetric patterns create deviations that are not easily determined and modeled. Closing this gap will necessitate simultaneous in vivo experimentation with real-time molecular profiling to assess the accuracy of simulation predictions especially with respect to mixed-field and chronic low dose rate exposure conditions.

Developing hybrid multi-organism exposure models that can simulate cross-tissue communications, immune system interactions, and metabolic feedback during radiation exposure acclimatization should be a priority in future studies. If integrated into predictive computational twins, these models can potentially allow the real-time assessment of the cell health index and cellular repair states over time. Adding tiered adaptive AI systems for multifunctional concurrent computing would offer real-time data on ex vivo, in vivo, and whole-systems responses, easing the transition from cell culture to organism-level simulations. At the same time, the design of both active and passive radiation shielding should be updated to include effectiveness measures incorporating biological outcome metrics, not solely framework physical dose reductions. Such cross-disciplinary endeavors would underpin the quantitative metrics for next-generation countermeasure development, which would then be employed to keep astronauts safe and mission achievable for ever more ambitious interplanetary exploration initiatives.

References

1. Kennedy, Ann R. "Biological effects of space radiation and development of effective countermeasures." *Life sciences in space research* 1 (2014): 10-43.
2. Cucinotta, Francis A. "Space radiation risks for astronauts on multiple International Space Station missions." *PloS one* 9.4 (2014): e96099.
3. O'Neill, Patrick M. "Badhwar–O'Neill galactic cosmic ray model update based on advanced composition explorer (ACE) energy spectra from 1997 to present." *Advances in Space Research* 37.9 (2006): 1727-1733.
4. Hu, Shaowen. "Solar particle events and radiation exposure in space." *NASA Space Radiation Program Element, Human Research Program* (2017): 1-15.
5. Hands, Alex DP, et al. "Radiation effects on satellites during extreme space weather events." *Space Weather* 16.9 (2018): 1216-1226.
6. Zeitlin, C., et al. "Measurements of energetic particle radiation in transit to Mars on the Mars Science Laboratory." *science* 340.6136 (2013): 1080-1084.

7. Huang, Ruixue, and Ping-Kun Zhou. "DNA damage repair: historical perspectives, mechanistic pathways and clinical translation for targeted cancer therapy." *Signal transduction and targeted therapy* 6.1 (2021): 254.
8. Azzam, Edouard I., Jean-Paul Jay-Gerin, and Debkumar Pain. "Ionizing radiation-induced metabolic oxidative stress and prolonged cell injury." *Cancer letters* 327.1-2 (2012): 48-60.
9. Lomax, Martine E., Lisa K. Folkes, and Peter O'Neill. "Biological consequences of radiation-induced DNA damage: relevance to radiotherapy." *Clinical oncology* 25.10 (2013): 578-585.
10. Radstake, Wilhelmina E., et al. "DNA double-strand break repair kinetics after exposure to photons and ions: a systematic review." *Radiation Research* 201.6 (2024): 604-616.
11. Hu, Ankang, et al. "Modeling of DNA damage repair and cell response in relation to p53 system exposed to ionizing radiation." *International Journal of Molecular Sciences* 23.19 (2022): 11323.
12. Cordoni, Francesco G. "A spatial measure-valued model for radiation-induced DNA damage kinetics and repair under protracted irradiation condition." *Journal of Mathematical Biology* 88.2 (2024): 21.
13. Zaharieva, Elena K., Megumi Sasatani, and Kenji Kamiya. "Kinetics of DNA repair under chronic irradiation at low and medium dose rates in repair proficient and repair compromised normal fibroblasts." *Radiation Research* 197.4 (2022): 332-349.
14. Pariset, Eloise, et al. "DNA damage baseline predicts resilience to space radiation and radiotherapy." *Cell reports* 33.10 (2020).
15. Goodhead, Dudley T. "Initial events in the cellular effects of ionizing radiations: clustered damage in DNA." *International journal of radiation biology* 65.1 (1994): 7-17.
16. Rudolf, Agata M., and Wendy R. Hood. "Mitochondrial stress in the spaceflight environment." *Mitochondrion* 76 (2024): 101855.
17. da Silveira, Willian A., et al. "Comprehensive multi-omics analysis reveals mitochondrial stress as a central biological hub for spaceflight impact." *Cell* 183.5 (2020): 1185-1201.
18. Mitchell, Adam, et al. "Cardiovascular effects of space radiation: implications for future human deep space exploration." *European Journal of Preventive Cardiology* 26.16 (2019): 1707-1714.
19. Cherry, Jonathan D., et al. "Galactic cosmic radiation leads to cognitive impairment and increased aβ plaque accumulation in a mouse model of Alzheimer's disease." *PloS one* 7.12 (2012): e53275.
20. Parousis-Paraskevas, Orfeas, et al. "Combined Radiations: Biological Effects of Mixed Exposures Across the Radiation Spectrum." *Biomolecules* 15.9 (2025): 1282.
21. Guéguen, Yann, Alice Bontemps, and Teni G. Ebrahimian. "Adaptive responses to low doses of radiation or chemicals: their cellular and molecular mechanisms." *Cellular and Molecular Life Sciences* 76.7 (2019): 1255-1273.
22. Kokhan, Viktor S., and Mikhail I. Dobynde. "The effects of galactic cosmic rays on the central nervous system: from negative to unexpectedly positive effects that astronauts may encounter." *Biology* 12.3 (2023): 400.
23. McCoy, Margaret A., et al., eds. "Review of NASA's Evidence Reports on Human Health Risks: 2014 Letter Report." (2015).
24. Cucinotta, Francis A., et al. "Benchmarking risk predictions and uncertainties in the NSCR model of GCR cancer risks with revised low LET risk coefficients." *Life Sciences in Space Research* 27 (2020): 64-73.